Published in final edited form as:
Nat Struct Mol Biol. 2023 February ; 30(2): 188–199. doi:10.1038/s41594-022-00909-1.

Structural maturation of SYCP1-mediated meiotic chromosome synapsis by SYCE3

James H. Crichton[#1], **James M. Dunce**[#2,3], **Orla M. Dunne**[2,4], **Lucy J. Salmon**[2], **Paul S. Devenney**[1], **Jennifer Lawson**[1], **Ian R. Adams**[1], **Owen R. Davies**[2,5]

[1]MRC Human Genetics Unit, MRC Institute of Genetics and Cancer, University of Edinburgh, Crewe Road South, Edinburgh, EH4 2XU, UK

[2]Biosciences Institute, Faculty of Medical Sciences, Newcastle University, Framlington Place, Newcastle upon Tyne NE2 4HH, UK

[5]Wellcome Centre for Cell Biology, Institute of Cell Biology, University of Edinburgh, Michael Swann Building, Max Born Crescent, Edinburgh EH9 3BF

[#] These authors contributed equally to this work.

Abstract

In meiosis, a supramolecular protein structure, the synaptonemal complex (SC), assembles between homologous chromosomes to facilitate their recombination. Mammalian SC formation is thought to involve hierarchical zipper-like assembly of an SYCP1 protein lattice that recruits stabilising central element (CE) proteins as it extends. Here, we combine biochemical approaches with separation-of-function mutagenesis in mice to show that, rather than stabilising the SYCP1 lattice, the CE protein SYCE3 actively remodels this structure during synapsis. We find that SYCP1 tetramers undergo conformational change into 2:1 heterotrimers upon SYCE3-binding, removing their assembly interfaces and disrupting the SYCP1 lattice. SYCE3 then establishes a new lattice by its self-assembly mimicking the role of the disrupted interface in tethering together SYCP1 dimers. SYCE3 also interacts with CE complexes SYCE1-SIX6OS1 and SYCE2-TEX12, providing a mechanism for their recruitment. Thus, SYCE3 remodels the SYCP1 lattice into a CE-binding integrated SYCP1-SYCE3 lattice to achieve long-range synapsis by a mature SC.

Correspondence to: Ian R. Adams; Owen R. Davies.

Authors for Correspondence: Ian Adams: Ian.Adams@ed.ac.uk; Owen Davies: Owen.Davies@ed.ac.uk.
[3]Current address: Department of Biochemistry, University of Cambridge, 80 Tennis Court Road, Old Addenbrookes Site, Cambridge CB2 1GA, UK.
[4]Current address: Vienna BioCenter Core Facilities GmbH, Dr. Bohr-Gasse 3, 1030 Vienna, Austria.

Author contributions statement
J.M.D., O.M.D. and L.J.S. performed biochemical and biophysical experiments. J.H.C. performed mouse phenotyping, developed imaging analysis pipelines and analysed imaging. P.D. performed CRISPR/Cas9 injections. J.L. performed mouse genotyping. O.R.D. and I.R.A. analysed data, designed experiments and wrote the manuscript.

Competing interests statement
The funders had no role in study design, data collection and analysis, decision to publish or preparation of the manuscript. The authors declare no competing interests.

Animal Ethics
Experiments involving animals were conducted in line with institutional and national ethical and welfare guidelines and regulations. The experiments described in this study were approved by the University of Edinburgh animal welfare and ethics review board and performed under authority of UK Home Office licences PP3007F29 and PB0DC8431.

Keywords

Meiosis; recombination; synaptonemal complex; SYCP1; SYCE3; self-assembly; small-angle X-ray scattering; mouse; bioimage analysis

Introduction

In meiosis, haploid germ cells are formed through the segregation of homologous chromosomes following their genetic exchange by crossing over. This requires a supramolecular protein structure, the synaptonemal complex (SC), which binds homologous chromosomes together, in synapsis, to facilitate recombination[1,2]. SC assembly is directed by the inter-homologue alignments established at recombination intermediates formed at sites of induced double-strand breaks (DSBs)[3]. The mature SC structure then provides the necessary three-dimensional framework for DSB repair and crossover formation[1,2]. The structural integrity of the SC is essential for meiosis across eukaryotes[2], and SC defects are associated with human infertility, miscarriage and aneuploidy[4–6]. However, the mechanism of mammalian SC assembly remains poorly understood.

The SC is a ribbon-like structure of up to 24 μm length in humans[7], which assembles between aligned chromosome axes at typically 400 nm initial separation, and brings their parallel axes into 100 nm synapsis[1,2]. Mammalian SC assembly is thought to occur via a hierarchical zipper-like mechanism[8,9]. Firstly, SYCP3-containing axial/lateral elements assemble along individual unaligned chromosome axes, which subsequently become aligned in homologous pairs by recombination. SYCP1 transverse filaments then assemble between aligned axes, organised with the C-termini of this coiled-coil protein within the lateral elements, and its N-termini within a midline central element (CE) (Fig. 1a)[10,11]. Head-to-head interactions between SYCP1's N-termini are reinforced by recruitment of CE proteins SYCE3, SYCE1-SIX6OS1, and finally SYCE2-TEX12, which confer stability to the SC and allow its extension along the chromosome axis to achieve full synapsis. This hierarchical zipper-like model for SC assembly is supported by analysis of mice carrying mutations in these SC proteins, which exhibit defects at the expected stages of SC assembly with failure to recruit downstream SC proteins, and resultant chromosome asynapsis, spermatocyte death and infertility in males[10,12–17].

Structural and biochemical analyses have generated significant insight into the molecular mechanisms and protein interactions at play within the SC[18–23]. The SC's underlying midline architecture is thought to be provided by an 'SYCP1 tetramer lattice' that can self-assemble *in vitro* and is stabilised by CE proteins *in vivo*[18]. In this lattice, SYCP1's α-helical core (amino-acids 101-783) has a tetrameric structure, in which two parallel SYCP1 dimers are bound together via a 'tetramer interface', located towards their N-termini, within a region defined as the αNcore (amino-acids 206-362) (Fig. 1b). These bifurcating molecules span between central and lateral elements, where they self-assemble through head-to-head interactions of their N-terminal α-helical tips (αNtips; amino-acids 101-111), and back-to-back interactions between DNA-binding C-termini (Fig. 1a,b). Individual αNtip interactions are weak, likely to enable synaptic adjustment, meaning that head-to-head

interactions depend on the cooperativity afforded through the tethering together of adjacent αNtip dimers into a lattice structure by the tetramer interface (Fig. 1a,b). Thus, αNtip interactions and the tetramer interface combine into an 'SYCP1 tetramer lattice' that binds together chromosome axes and seemingly defines the midline structure of the SC (Fig. 1a,b)[18].

Whilst SYCP1 is sufficient for SC-like lattice assembly *in vitro*[18,24], the formation of a structurally and functionally mature SC is entirely dependent on recruitment of CE proteins SYCE3, SYCE1-SIX6OS1 and SYCE2-TEX12 *in vivo*[13–17]. It has been proposed that CE proteins stabilise short- and long-range interactions within the SYCP1 lattice, including through their self-assembly[9,18]. Indeed, SYCE3 is a dimer that self-assembles through hierarchical end-on and lateral interactions of its coiled-coil structure[20], and is thought to stabilise short-range interactions of synapsis[14]. Further, SYCE2-TEX12 self-assembles into micrometre fibres that are thought to constitute the backbone of the SC, supporting its longitudinal growth along the chromosome length[13,16,23]. However, it remains unknown how CE proteins interact and integrate with the SYCP1 tetramer lattice to drive its extension along the chromosome length during SC assembly *in vivo*.

Here, we combine *in vitro* biochemical and structural studies, with genetics and imaging analysis of a separation-of-function mouse mutation *in vivo*, to uncover that SYCE3 has an essential role in actively remodelling SYCP1 tetramer lattices during the early stages of synapsis. We find that SYCE3-binding directly competes with SYCP1's tetramer interface, disrupting the SYCP1 tetramer lattice. SYCE3 self-assembly then compensates for the disrupted interface by supporting formation of a new integrated SYCP1-SYCE3 lattice. Further, SYCE3 binds directly to CE complexes SYCE1-SIX6OS1 and SYCE2-TEX12, providing a means for their recruitment. Thus, SYCE3 acts as a molecular adapter, remodelling the nascent SYCP1 tetramer lattice into a CE-binding integrated SYCP1-SYCE3 lattice to achieve structural and functional maturation of the mammalian SC.

Results

The tetrameric core of SYCP1 binds to SYCE3

How do nascent SYCP1 assemblies become stabilised and extended into a mature SC? We screened for interactions between SYCP1 and individual CE proteins by yeast two-hybrid (Y2H), revealing that SYCP1 binds to SYCE3 (Fig. 1c,d). This agrees with a separate study[25], and is consistent with SYCE3's early role in hierarchical SC assembly[14]. We confirmed this interaction by pull-down of recombinant proteins and identified the SYCE3-binding site of SYCP1 as its tetrameric core (amino-acids 206-362, herein referred to as SYCP1αNcore; Fig. 1e). SYCP1αNcore lies at the N-terminal end of SYCP1's parallel coiled-coil dimers, and includes the tetramer interface that binds them together, but lacks the upstream αNtip sites that are necessary for head-to-head assembly (Fig. 1b). Co-expressed SYCP1αNcore and SYCE3 purified as a stable complex that co-migrated as a distinct single species on size-exclusion chromatography (Fig. 1f,g and Extended Data Fig. 1a,b). Isothermal calorimetry (ITC) of the same complex, formed by mixing its purified components (Fig. 1f and Extended Data Fig. 1b), indicated a binding affinity of 170 ± 30 nM (Fig. 1h and Extended Data Fig. 1c). Thus, SYCP1's tetrameric core binds with

nanomolar affinity to SYCE3, implicating this region of SYCP1 in hierarchical assembly of the SC central element (Fig. 1i).

The SYCP1 tetramer interface is disrupted by SYCE3

We expected that SYCE3 would stabilise the SYCP1 tetramer interface to support a combined role with αNtip sites in tetramer lattice formation. In contrary, size-exclusion chromatography multi-angle light scattering (SEC-MALS) identified that SYCP1αNcore-SYCE3 is a 2:1 hetero-trimer (Fig. 2a and Extended Data Fig. 2a). This indicates that SYCP1αNcore and SYCE3 are remodelled from tetramers and dimers upon interaction, with SYCE3-binding disrupting the SYCP1 tetramer interface. SYCP1's full α-helical core, in which αNtips were deleted to prevent lattice assembly (amino-acids 112-783; Fig. 1b), was similarly remodelled from a tetramer to a 2:1 complex by SYCE3-binding (Extended Data Fig. 2b). Thus, disruption of the tetramer interface within SYCP1αNcore represents the structural consequence of SYCE3-binding to the wider SYCP1 molecule.

How is SYCP1 remodelled into a 2:1 complex upon SYCE3-binding? The SYCP1αNcore tetramer and 2:1 complex are almost entirely α-helical and have similar melting temperatures (Extended Data Fig. 2c,d), indicating their comparable structural stability, consistent with them both having biological roles. Small-angle X-ray scattering (SAXS) determined that both species have rod-like geometries, which are consistent with the theoretical 240 Å length of an extended SYCP1αNcore coiled-coil, and the known cross-sectional radii of tetrameric and trimeric coiled-coils, respectively (Fig. 2b and Extended Data Fig. 2e-g). Thus, SYCE3-binding remodels SYCP1αNcore from an extended tetrameric coiled-coil into an extended 2:1 hetero-trimeric coiled-coil of equivalent structural stability.

SYCE3 is a dimer of helix-loop-helix chains locked in a four-helical conformation, which self-assembles into higher-order structures (Fig. 2c,d)[20,26]. As both helices are required for SYCP1-binding (Extended Data Fig. 2h), we wondered whether SYCE3's helix-loop-helix conformation is retained within the 2:1 complex. In SYCE3 self-assembly, chains are remodelled from helix-loop-helix to extended α-helical conformations – promoted by P53Q mutation and blocked by 'PPP-loop' mutation – such that they bridge between end-on dimers in a 'domain-swap' fashion (Fig. 2d and Extended Data Fig. 3a)[20]. The resultant SYCE3 tetramers then assemble into higher-order structures through lateral interactions that are blocked by a W41E Y44E (WY) mutation (Fig. 2d and Extended Data Fig. 3a)[20]. 2:1 complex formation was retained in P53Q and WY mutants, with SYCE3 WY binding to SYCP1αNcore with higher affinity than wild-type (K_D = 16 ± 3 nM) (Fig. 2g and Extended Data Fig. 3b). In contrast, the interaction was abrogated by the PPP-loop mutation (Fig. 2e,f and Extended Data Fig. 3c). Thus, our mutational analysis indicates that the SYCE3 chain within the 2:1 complex adopts the extended α-helical conformation that supports SYCE3 self-assembly, rather than the helix-loop-helix conformation of the SYCE3 dimer.

In summary, SYCE3-binding and SYCP1 tetramer formation are mutually exclusive. SYCE3 forms a hetero-trimeric coiled-coil with SYCP1αNcore, competitively inhibiting the tetramer interface, and thereby remodelling an SYCP1 tetramer into SYCE3-bound dimers

(Fig. 2h). Hence, SYCE3 disrupts rather than stabilises SYCP1 tetramers, so is predicted to inhibit SYCP1 tetramer lattice formation.

SYCP1-SYCE3 undergoes αNtip-mediated head-to-head assembly

SYCP1αNcore is restricted to forming a tetramer as it lacks the αNtip sites that mediate head-to-head assembly. In contrast, SYCP1's full α-helical N-terminal region (amino-acids 101-362, herein referred to as SYCP1αN; Fig. 1b) contains both αNtips and the tetramer interface, so undergoes higher-order assembly (representing tetramer lattice formation) *in vitro*[18]. Thus, to test whether SYCE3 inhibits SYCP1 tetramer lattice formation, we analysed the complex between SYCP1αN and SYCE3. SEC-MALS determined that co-expressed SYCP1αN-SYCE3 formed higher-order assemblies, in a range of molecular weights up to those observed for SYCP1αN in isolation (Fig. 3a). Further, upon titration into SYCP1αN, SYCE3 was recruited to SYCP1αN assemblies, with little disruption at ten-fold molar excess (Extended Data Fig. 4a). Higher-order assembly was blocked upon deletion of αNtip or introduction of mutation V105E L109E that disrupts αNtip head-to-head interactions[18], with SYCP1αN-SYCE3 restricted to a stable 2:1 complex (Fig. 3a and Extended Data Fig. 4a). Thus, αNtip-mediated higher-order assembly of SYCP1αN is retained upon SYCE3-binding.

If SYCP1αN-SYCE3 assembles through the same αNtip head-to-head interactions that are responsible for SYCP1 tetramer lattice assembly, then we would predict the presence of an assembly intermediate in which 2:1 species interact 'head-to-head' in 4:2 complexes. Accordingly, upon selective purification to remove higher-order species, we determined that the lowest molecular weight species of SYCP1αN-SYCE3 correspond to 2:1 and 4:2 complexes (Fig. 3b). In support of this, the MBP-fusion complex formed only 2:1 and 4:2 species, likely owing to inhibition of higher-order assembly by steric hindrance (Extended Data Fig. 4b). SAXS analysis of the 2:1 and 4:2 complexes revealed rod-like molecules in which 4:2 complexes are almost twice as long as 2:1 complexes, consistent with their formation through end-on interactions of 2:1 complexes (Fig. 3c,d and Extended Data Fig. 4c,d). Thus, we conclude that higher-order assembly, mediated by αNtip head-to-head interactions, is retained upon SYCE3 binding to SYCP1αN, despite disruption of the tetramer interface.

An integrated lattice is established by SYCE3 self-assembly

How does SYCP1αN-SYCE3 undergo αNtip-mediated assembly in absence of the tetramer interface? The SYCE3 WY mutation, which blocks lateral interactions of the SYCE3 self-assembly pathway (Fig. 2d), also blocked higher-order assembly and restricted SYCP1αN-SYCE3 to a 2:1 complex, despite the presence of αNtips (Fig. 3e). The ability to block SYCP1αN assembly by deleting the αNtip[18], or disrupting the tetramer interface by SYCE3 WY-binding (Fig. 3e), is consistent with the tetramer interface providing the cooperativity necessary to support individually weak αNtip interactions. Further, these data suggest that SYCE3's lateral assembly interactions must compensate for the missing tetramer interface between SYCP1 dimers by providing an analogous 'tetramer-like' interface between adjacent SYCE3-bound SYCP1 dimers.

The addition of free SYCE3 to SYCP1αN-SYCE3 2:1 and 4:2 complexes triggered their assembly into higher-order species in a manner that was blocked by the WY mutation (Fig. 3f and Extended Data Fig. 5a,b). Thus, 'tetramer-like' interfaces provided by SYCE3's lateral assembly interactions likely involve SYCP1-SYCE3 2:1 complexes being linked together by additional SYCE3 molecules, rather than by direct interactions. Given the shared SYCE3 extended chain conformation, we wondered whether SYCP1-SYCE3 2:1 complexes may structurally mimic SYCE3 tetramers, allowing their incorporation as laterally-interacting units within SYCE3 assemblies. This explains disruption by the WY mutation, and predicts that 'tetramer-like' interfaces are independent of αNtips. Accordingly, SYCP1αNcore-SYCE3, which lacks αNtips and forms only 2:1 complexes in isolation, underwent higher-order assembly upon addition of free SYCE3, but not of the WY mutant (Fig. 3g,h and Extended Data Fig. 5c). As these structures form through lateral assembly interactions, they may include more than two SYCP1-SYCE3 2:1 complexes, linked together by a variable quantity of SYCE3 molecules, explaining the range of molecular weight species observed in solution (Fig. 3g-i). In addition to these lateral assembly interactions, SYCP1αN-SYCE3 also undergoes αNtip-mediated head-to-head assembly, enabling the formation of lattice assemblies. Hence, we conclude that SYCP1-SYCE3 forms an integrated lattice, in a similar manner to the SYCP1 tetramer lattice, through cooperativity between αNtip head-to-head interactions and 'tetramer-like' interfaces between SYCE3-bound SYCP1 dimers mediated by their lateral incorporation into SYCE3 assemblies (Fig. 3i).

In summary, our findings suggest that SYCE3 remodels the SYCP1 tetramer lattice into a structurally distinct integrated SYCP1-SYCE3 lattice (Fig. 3i). Firstly, SYCE3-binding disrupts SYCP1's tetramer interface, dissolving the tetramer lattice into SYCP1-SYCE3 2:1 complexes. Then, SYCE3 assemblies link together 2:1 molecules, mimicking the disrupted tetramer interface, to support cooperative αNtip head-to-head interactions within an integrated SYCP1-SYCE3 lattice (Fig. 3i).

Syce3$^{WY/WY}$ mice are infertile with failure of SC assembly

We next investigated how the ability of SYCE3 to remodel SYCP1 tetramer lattices *in vitro* relates to SC assembly *in vivo*. The SYCE3 WY mutation separates the disruptive and integrative functions of SYCE3, triggering SYCP1 tetramer lattice disruption, whilst failing to form an integrated SYCP1-SYCE3 lattice (Fig. 3i). Hence, the WY mutation is predicted to be more deleterious than a simple SYCE3 deletion, in which SYCP1 tetramer lattices can be retained but cannot be remodelled (Fig. 3i). Thus, to test our model for SYCP1 lattice remodelling by SYCE3, we generated and analysed SC assembly in *Syce3*$^{WY/WY}$ mice.

As *Syce3*^{WY} has the potential to act in a dominant-negative manner, we circumvented the need for fertile *Syce3*$^{WY/+}$ heterozygotes by analysing *Syce3*$^{WY/WY}$ homozygotes born directly from CRISPR/Cas9 gene editing in zygotes (Fig. 4a)[27,28]. We also generated control *Syce3*$^{PAM/PAM}$ mice possessing the silent protospacer adjacent motif (PAM) mutations introduced alongside the WY mutation in *Syce3*$^{WY/WY}$ mice, and *Syce3*$^{\Delta/\Delta}$ mice carrying *Syce3* frameshift deletions preceding or encompassing the WY mutation site as potential null alleles (Fig. 4a,b and Extended Data Fig. 6a,b). The *Syce3*$^{PAM/PAM}$ control mice,

which encode wild-type SYCE3 protein, control for off-target CRISPR/Cas9 editing events and unexpected effects of the synonymous and non-coding PAM site mutations on *SYCE3* expression.

Syce3$^{WY/WY}$ and *Syce3*$^{\Delta/\Delta}$ homozygotes exhibited severely reduced testis weights and epididymal sperm counts, with testis histology indicating a severe block in meiosis, whereas *Syce3*$^{PAM/PAM}$ homozygotes had no overt defects (Fig. 4c,d)[29]. Furthermore, no overt phenotypic mosaicism was detected in these animals (Fig. 4c,d). Immunostained chromosome spreads demonstrated that RAD51 recombination foci formed in *Syce3*$^{WY/WY}$ and *Syce3*$^{\Delta/\Delta}$ spermatocytes (Fig. 4e), but extensive regions of SYCP3-coated chromosome axes did not synapse and SYCP1 recruitment was fragmented (Fig. 4f), with meiosis arrested at pachytene (Extended Data Fig. 6c). These findings correlate with the reported *Syce3*$^{-/-}$ phenotype[14], confirming that SYCE3's W41/Y44-mediated lateral self-assembly interactions are essential for *Syce3* function and SC assembly *in vivo*. Thus, the nature and severity of the *Syce3*$^{WY/WY}$ phenotype are consistent with our biochemical findings and support our model for SC assembly through SYCP1 lattice remodelling by SYCE3.

SYCP1 assembly is severely disrupted in *Syce3*$^{WY/WY}$ mice

Although fragmented SYCP1 staining was detected on chromosome axes in both *Syce3* mutants, SYCP1 staining was considerably less prominent in *Syce3*$^{WY/WY}$ than *Syce3*$^{\Delta/\Delta}$ nuclei, requiring a 10-fold increase in image brightness for detection (Fig. 4f). This more deleterious effect of *Syce3*^{WY} than *Syce3* null alleles on SYCP1 assembly presumably reflects the ability of SYCE3 to disrupt the SYCP1 tetramer lattice. We therefore examined their SYCP1 foci in detail using structured illumination microscopy (SIM). In *Syce3*$^{PAM/PAM}$ pachytene nuclei, SYCP1 localised between pairs of SYCP3-stained axes, often appearing as chains of foci separated by a central gap (consistent with its biorientation), with occasional discontinuities, and sometimes as linear extensions tightly associated with one of the axes (Fig. 5a and Extended Data Fig. 7a). In asynapsed *Syce3*$^{WY/WY}$ and *Syce3*$^{\Delta/\Delta}$ pachytene nuclei, SYCP1 staining was less orderly, consisting of mostly axial foci (within 35 nm of the SYCP3 axis; Extended Data Fig. 7b), and we rarely observed extensive chains of foci linking paired axes (Fig. 5a-c). In agreement with widefield imaging, the number and intensity of both axial and non-axial SYCP1 foci were far greater in *Syce3*$^{\Delta/\Delta}$ than *Syce3*$^{WY/WY}$ nuclei (Fig. 5c,d and Extended Data Fig. 7b-e). Thus, the SYCP1 foci present in *Syce3*$^{\Delta/\Delta}$ nuclei likely include SYCP1 tetramer lattices whose assembly and/or stability are actively disrupted by the SYCE3 WY mutation.

We next investigated whether the SYCP1 tetramer lattices in *Syce3*$^{\Delta/\Delta}$ spermatocytes resemble mature SCs, in which extensive chains of SYCP1 foci bridge between synapsed axes (Fig. 5a), by focussing on large extended SYCP1 assemblies at sites of close proximity between paired SYCP3 axes. In some cases, these large extended SYCP1 foci consisted of linear structures associated with tightly apposed SYCP3 axes, or were assembled in the gap between pairs of SYCP3 axes, but did not appear to consist of extensive chains of foci seen in synapsed control spermatocytes (Fig. 5e, panel i-iii). In other cases, the large extended SYCP1 foci were composed of paired linear SYCP1 assemblies extending separately along each axis, potentially separated in places by a central gap (Fig. 5e, panels iv-v). Whilst

SYCP1 appears to be unable to assemble into extensive chains of foci in the absence of SYCE3, these extending linear SYCP1 assemblies resemble the linear extensions of SYCP1 observed in some regions of the mature SC (Extended Data Fig. 7a). Thus, SYCP1 tetramer lattices can contribute to the SYCP1 assemblies between closely paired SYCP3 axes, but lattice remodelling by SYCE3 is required for assembly of SYCP1 into the extensive chains of foci seen in the mature SC.

In summary, *Syce3* mutants exhibit defects at distinct SC assembly stages that support our biochemical findings and model for SYCP1 lattice remodelling by SYCE3. Firstly, $Syce3^{\Delta/\Delta}$ captures the formation of SYCP1 tetramer lattices between axes, which cannot be remodelled in absence of SYCE3, so fail to develop into a mature SC (Fig. 5f). Secondly, $Syce3^{WY/WY}$ captures the stage at which SYCP1 tetramer lattices are disrupted by SYCE3 but cannot be remodelled into integrated SYCP1-SYCE3 lattices (Fig. 5f). Finally, in wild-type and control $Syce3^{PAM/PAM}$ mice expressing wild-type SYCE3 protein, SYCE3 remodels SYCP1 tetramer lattices into integrated SYCP1-SYCE3 lattices that support full SC maturation (Fig. 5f).

SYCE3 recruits SYCE1-SIX6OS1 and SYCE2-TEX12 complexes

What is the functional consequence of SYCE3 integration into the SYCP1 lattice? The CE contains three high-affinity ‘building-block’ complexes: SYCP1-SYCE3 (this study), SYCE1-SIX6OS1[21] and SYCE2-TEX12[23]. We identified through biochemical pull-downs that SYCE3 binds to SYCE1-SIX6OS1 and SYCE2-TEX12 complexes (Fig. 6a-d). The SYCE1-SIX6OS1 interaction is mediated by SYCE3’s N-terminus binding to SYCE1’s α-helical core (Fig. 6a,b), whilst the SYCE2-TEX12 interaction requires the presence of both SYCE2 and TEX12 components (Fig. 6d). In both cases, complexes largely dissociated during size-exclusion chromatography (Fig. 6e and Extended Data Fig. 8a,b), consistent with micromolar binding affinities. Indeed, microscale thermophoresis identified a binding affinity between SYCE3 and SYCE2-TEX12 of 22 ± 2 μM (Fig. 6f and Extended Data Fig. 8c-i). These SYCE3 interactions are two orders of magnitude weaker than constituent interactions of the SC’s core complexes, suggesting that they are dynamic, with rapid turnover of binding partners, and likely achieve stability through cooperativity within the SC lattice. Further, SYCE3 promoted fibrous assembly of SYCE2-TEX12 (Fig. 6g and Extended Data Fig. 9), suggesting that it functions both in the recruitment and assembly of the CE.

Our data suggest that SYCE3 acts as a molecular adapter that binds together the CE’s ‘building-block’ complexes, through a combination of high- and low-affinity binding interfaces, and self-assembly interactions, to assemble a mature SC structure (Fig. 6h). SYCE3 remodels and integrates into the SYCP1 lattice, establishing binding sites that cooperativity recruit SYCE1-SIX6OS1 and SYCE2-TEX12, and stimulate SYCP1-SYCE3 and SYCE2-TEX12 assembly, to structurally reinforce and drive SC growth (Fig. 7). This model explains the failed extension of SYCP1 assemblies in $Syce3^{\Delta/\Delta}$ nuclei, and the severe disruption of SYCP1 assemblies in $Syce3^{WY/WY}$. Hence, we uncover an essential role for SYCE3 in integrating the CE’s distinct architectural units into a structurally and functionally mature SC.

Discussion

Our combined biochemical and separation-of-function mutagenesis studies provide a new paradigm for the role of CE protein SYCE3 in mammalian SC assembly. Firstly, rather than simply stabilising existing SYCP1 assemblies, SYCE3 remodels the SYCP1 tetramer lattice into an integrated SYCP1-SYCE3 lattice that enables SC growth (Fig. 7). Secondly, SYCE3 promotes SYCP1-SYCE3 lattice extension and SYCE2-TEX12 fibre formation through SYCP1, SYCE3 and SYCE2-TEX12 self-assembly. Finally, SYCE3 is central within a network of low-affinity interactions that bind together the SC's high-affinity heteromeric complexes SYCP1-SYCE3, SYCE1-SIX6OS1 and SYCE2-TEX12 (Fig. 6h). Thus, SYCE3 performs multiple distinct roles as a molecular adapter of SC assembly.

The remodelling of SYCP1 tetramer lattices into integrated SYCP1-SYCE3 lattices involves multiple conformational remodelling and self-assembly mechanisms. Upon binding, SYCP1 and SYCE3 undergo conformational change from tetramers and dimers to a 2:1 hetero-trimeric complex, in a process that competes with, and thereby disrupts, SYCP1's tetramer interface. In parallel, SYCE3 self-assembles by conformational domain-swap of dimers into tetramers that interact laterally (Fig. 2d)[20]. These SYCE3 assemblies bind to, and link together, SYCP1-SYCE3 complexes, mimicking the role of the disrupted tetramer interface to establish a new integrated SYCP1-SYCE3 lattice (Fig. 7). The number of SYCE3 molecules within each assembly is likely variable, and may incorporate multiple SYCP1-SYCE3 complexes. Hence, we envisage a heterogeneous system in which the distance between SYCP1-SYCE3 complexes and the extent of SYCE3-mediated lateral assemblies may adapt to the local structure of chromosome axes. Thus, SYCP1 and SYCE3 exhibit conformational plasticity, with the same protein sequences forming multiple distinct conformations and assemblies. The formation of alternative conformations has been observed in other coiled-coil systems, and is attributed to their similar interfaces giving rise to only small differences in the free-energy of folding[30–32]. Hence, this plasticity is likely consequential of the coiled-coil nature of SC proteins.

Are the SYCP1 tetramer lattice and integrated SYCP1-SYCE3 lattice temporally exclusive or could they co-exist within an assembled SC? The similar melting temperatures of SYCP1αNcore and its complex with SYCE3 suggest that both lattices have similar stability. Thus, the SC could be sustained locally by either lattice type, which could be dynamically and reversibly remodelled through active or reactive mechanisms such as local SYCE3 availability and post-translational modifications[33]. A more adaptive SYCP1 tetramer lattice may be required to enable synaptic adjustment of initially poorly aligned axes prior to formation of a mature SC structure, whereas the SYCP1-SYCE3 lattice may represent a more rigid structure (Fig. 7). The structural heterogeneity that would result from the co-existence of both lattice types is consistent with the irregularities in SYCP1 structures observed within the assembled mouse SC by immunofluorescence (Fig. 5a and Extended Data Fig. 7a) and EM[34]. Further, the distinct SYCP1 tetramer and integrated SYCP1-SYCE3 lattice structures may have functional consequence, such as permitting differential access to recombination sites as a means of locally regulating meiotic recombination. This may explain the observed structural alterations of the SC at recombination sites in *C. elegans*[35,36]. Thus, it be of great interest to determine whether structural heterogeneity

and/or dynamic structural remodelling of the SC influence recombination frequencies and crossover outcomes in mammals.

The large axial SYCP1 foci formed in *Syce3*$^{\Delta/\Delta}$ but not *Syce3*$^{WY/WY}$ spermatocytes likely represent SYCP1 tetramer lattices that were trapped owing to the lack of SYCE3 (Fig. 5f). Whilst some assembled between paired axes at sites of potential synapsis, others were located on individual axes, raising the question of how SYCP1 tetramer lattices can assemble on single rather than paired axes. As SYCP1 assembles into tetramer lattices in absence of DNA *in vitro*[18,24], one side of the lattice may bind to the axis, leaving the other free to subsequently capture the paired axis (Fig. 5f). Alternatively, SYCP1 tetramer lattices may assemble between chromatin loops or sister chromatids of the same axis. Hence, SYCE3-binding may have an additional role in redirecting SYCP1 lattices towards inter-homologous synapsis. As SYCP1 assemblies on individual axes are also present in *Syce1*$^{-/-}$, but are rare in *Syce2*$^{-/-}$ spermatocytes[14,16,17], this likely involves the stabilising interactions of SYCE2-TEX12 proteins affording a cooperativity that strongly favours the formation of a single continuous inter-axial lattice rather than short discontinuous patches within individual axes.

The interaction network of the SC, which we defined through biochemical and biophysical analysis of recombinant SC proteins (Fig. 6h)[18,21], agrees with previous knockout phenotypes, co-immunoprecipitation and heterologous co-localisation studies[10,12–17,25,26]. Our findings reveal an apparent dichotomy of high-affinity (nanomolar) CE complexes – SYCP1-SYCE3, SYCE1-SIX6OS1 and SYCE2-TEX12 – that are held together by low-affinity (micromolar) interactions. This divides the SC's interactions into long-lasting complexes that likely represent its 'building-block' structures, and those that are transient and rapidly exchanged within a dynamic SC assembly. Further, SYCP1, SYCE3 and SYCE2-TEX12 undergo self-assembly through the cooperative action of similarly low-affinity individual interfaces (Fig. 6h)[18,23]. Hence, SYCP1-SYCE3, SYCE1-SIX6OS1 and SYCE2-TEX12 represent the SC's discrete heteromeric units that interact and self-assemble through low-affinity interfaces that are likely stabilised by cooperativity within the SC lattice. The SYCE3-mediated remodelling of the SYCP1 lattice raises the possibility that the SC undergoes further remodelling upon recruitment of other CE complexes. Given their comparative affinities, we speculate that SYCE3-binding by SYCE1-SIX6OS1 and SYCE2-TEX12 could affect the degree and nature of SYCE3 self-assembly, such as to control the number of SYCE3 proteins between adjacent SYCP1 molecules within an integrated SYCP1-SYCE3 lattice.

SC assembly involves two distinct SYCP1 lattices, which are interconverted by SYCE3 remodelling, and the binding together of its building-block complexes by low-affinity binary and self-assembly interactions. Together, these provide means for formation of a dynamic, adaptive and structurally heterogeneous SC from a series of well-defined and specific protein-protein interfaces. Indeed, the SC may be considered as having emergent functions[37], which could not be predicted from its individual protein components *a priori*, but are inherently defined by its constituent interactions. In this respect, active or passive remodelling of the SC may allow rapid bending, twisting and distortion of the central element in adaptation to mechanical stresses. This may influence accessibility

of recombination factors to recombining DNA, and dynamically regulate the frequency, distribution and outcomes of meiotic recombination. This functionality would not be possible if the SC had a homogenous and rigid structure. Hence, the complexity of interactions that underly the SC's structure are likely critically important to its function. Thus, the SC is one of the most intriguing and enigmatic biological structures, of which structural and functional understanding are critical to uncovering the molecular basis of meiotic recombination.

Methods

Recombinant protein expression and purification

SYCP1, SYCE3, SYCE1, SYCE1-SIX6OS1 and SYCE2-TEX12 protein constructs and complexes were purified as previously described[18–21,23,38]. In general, proteins were expressed as His- or His-MBP fusions in BL21(DE3) *E. coli* cells (Novagen®), and purified from lysate through Ni-NTA (Qiagen) or amylose (NEB) affinity, with removal of the tag by TEV protease treatment, followed by anion exchange chromatography (HiTrap Q HP, Cytiva) and size exclusion chromatography (HiLoad™ 16/600 Superdex™ 200, Cytiva) in 20 mM Tris pH 8.0, 150 mM KCl, 2 mM DTT. Purified proteins were concentrated using Amicon Ultra® 10,000 MWCO centrifugal filter units (Millipore) or Microsep™ Advance 3kDa (PALL) centrifugal filter units, and flash-frozen in liquid nitrogen for storage at -80°C. Samples were analysed by Coomassie-stained SDS-PAGE, and concentrations were determined using a Cary 60 UV spectrophotometer (Agilent) with molecular weights and extinction coefficients calculated by ExPASY ProtParam (http://web.expasy.org/protparam/).

Co-expression amylose pull-down assays

Protein-protein interactions of SYCE3 with SYCE1, SYCE1-SIX6OS1 and SYCE2-TEX12, were determined by co-expression pull-downs. In this, MBP fusions of the core constructs of SYCE1, SYCE1-SIX6OS1 and SYCE2-TEX12[19,21,38] were co-expressed with His- and GST-tagged SYCE3 constructs. For each construct, 3 l cultures were grown. Cells were lysed by sonication in 30 ml 20 mM Tris pH 8.0, 500mM KCl, and lysate clarified by high-speed centrifugation. The supernatant was applied to 6 ml amylose resin (NEB) at 4 °C. After washing with 30 ml 20 mM Tris pH 8.0, 150 mM KCl, 2 mM DTT, bound complexes were eluted in 20 mM Tris pH 8.0, 150 mM KCl, 2 mM DTT, 30 mM D-maltose. Sample concentrations were normalised and analysed by SDS-PAGE.

Co-purification interaction studies

The relative stability of SYCP1 and SYCE3 protein complexes was assessed by co-expression followed by stringent purification to determine their co-purification or dissociation. MBP-fusions of SYCP1 constructs were co-expressed with His-tagged SYCE3 constructs and were grown in 4 litre cultures, lysed and applied to 8ml amylose resin in 20 mM Tris pH 8.0, 500 mM KCl, 2 mM DTT. Amylose elutions were purified by anion exchange chromatography (HiTrap Q HP, Cytiva) and size exclusion chromatography (HiLoad™ 16/600 Superdex™ 200, Cytiva) in 20 mM Tris pH 8.0, 150 mM KCl, 2 mM DTT. MBP-SYCP1 elution fractions were pooled, and samples of equal concentrations were analysed by SDS-PAGE.

SYCP1-SYCE3 gel-filtration interaction studies

To analyse the SYCP1αNcore-SYCE3 interaction, 50 µl protein samples were prepared corresponding to SYCP1αNcore, SYCE3, the purified SYCP1αNcore-SYCE3 complex and a 1:1 mixture of SYCP1αNcore and SYCE3, with each component at 235 µM. To analyse the SYCP1αN-SYCE3 interaction, 50 µl protein samples were prepared corresponding to SYCP1αN, SYCE3 and mixtures of SYCP1αN and SYCE3 at 1:0.5, 1:5 and 1:10 molar ratios, in which the concentration of SYCP1αN was 127 µM. Samples were incubated for 1 hour at room temperature and centrifuged at 14000 g at 4˚C for 30 minutes. Size exclusion chromatography was performed using a Superdex™ 200 Increase 10/300 GL column in 20 mM Tris pH 8.0, 150 mM KCl, 2 mM DTT at 0.5 ml/min. Elution fractions were analysed by SDS-PAGE.

SYCP1-SYCE3 gel-filtration assembly assays

The SYCP1αNcore-SYCE3 complex was mixed with SYCE3 at a 10-fold molar excess (92 µM complex with 920 µM SYCE3 and SYCE3 W41E Y44E). SYCP1αN-SYCE3 complex was mixed with a 10-fold molar excess of SYCE3 (93 µM complex with 930 µM SYCE3 and SYCE3 W41E Y44E). Mixed samples and individual components were incubated for 1 hour at 30˚C and centrifuged at 14000 g at 4˚C for 30 minutes. Size exclusion chromatography was performed using a Superdex™ 200 Increase 10/300 GL (Cytiva) column in 20 mM Tris pH 8.0, 150 mM KCl, 2 mM DTT at 0.5 ml/min. Elution fractions were analysed by SDS-PAGE.

Circular dichroism (CD)

Far-UV CD spectra were measured using a Jasco J-810 spectropolarimeter (Institute for Cell and Molecular Biosciences, Newcastle University). Wavelength scans were measured at 4°C between 260 and 185 nm at 0.2 nm intervals at using a quartz cuvette, 0.2 mm pathlength (Hellma), with protein samples at 0.2-0.4 mg/ml in 10 mM Na2HPO4 pH 7.5, 150 mM NaF. For each sample, nine measurements were recorded, averaged and buffer corrected for conversion to mean residue ellipticity ([θ]) (x1000 deg.cm^2.dmol^{-1}.residue^{-1}) with deconvolution carried out using the Dichroweb CDSSTR algorithm (http://dichroweb.cryst.bbk.ac.uk). CD thermal melts were recorded between 5°C and 95°C, at intervals of 0.5°C with a 1°C per minute ramping rate, and measured at 222 nm. Protein samples were measured at 0.1 mg/ml in 20 mM Tris pH 8.0, 150 mM KCl, 2 mM DTT, in a 1 mm pathlength quartz cuvette (Hellma) and data plotted as % unfolded after conversion to MRE $([\theta]_{222,x}-[\theta]_{222,5})/([\theta]_{222,95}-[\theta]_{222,5})$ with melting temperatures determined as the temperature at which the samples are 50% unfolded.

Isothermal calorimetry (ITC)

ITC data were collected using a Malvern iTC200 instrument at 30°C on samples that had been dialysed overnight into 25 mM Tris pH 8.0, 250 mM KCl, 2 mM DTT, centrifuged at 14000 g at room temperature for 5 minutes, and degassed. SYCE3 (400 µM) was injected into the sample cell containing SYCP1αNcore (70 µM). 19 injections of 4 second duration and 2 µl volume (and an initial injection of 0.2 µl and 0.4 seconds) were performed at intervals of 240 seconds with stirring at 750 rpm. Data were integrated, fitted

and plotted using *NITPIC*[39], *SEDPHAT*[40] and GUSSI (https://www.utsouthwestern.edu/labs/mbr/software/), following reported protocols[41].

Microscale thermophoresis (MST)

Proteins were labelled in 10 mM HEPES pH 8.0, 150 mM NaCl using the Monolith NT Protein Labelling Kit RED (NanoTemper Technologies) according to the manufacturer's protocol. Labelled proteins were kept at a constant concentration indicated in the respective Figure legends. The unlabelled interacting partner was titrated in 1:1 dilutions. Measurements were performed in premium treated capillaries (NanoTemper Technologies) on a Monolith NT.115 system (NanoTemper Technologies) and excitation and MST power were set at 40 %. Laser on and off times were set at 5 and 30 seconds, respectively.

Size-exclusion chromatography multi-angle light scattering (SEC-MALS)

The oligomeric state of protein samples was determined by SEC-MALS analysis of protein samples at 5-20 mg/ml in 20 mM Tris pH 8.0, 150 mM KCl, 2 mM DTT. Samples were loaded at 0.5 ml/min onto a Superdex™ 200 Increase 10/300 GL (GE Healthcare) column with an ÄKTA™ Pure controlled by Unicorn software (GE Healthcare). The column outflow was fed into a DAWN® HELEOS™ II MALS detector (Wyatt Technology), and then an Optilab® T-rEX™ differential refractometer (Wyatt Technology). ASTRA® 6 software (Wyatt Technology) was used to collect and analyse SEC-MALS data, using Zimm plot extrapolation with a 0.185 ml/g dn/dc value to determine molecular weights from eluted protein peaks.

Size-exclusion chromatography small-angle X-ray scattering (SEC-SAXS)

SEC-SAXS experiments were performed on beamline B21 at Diamond Light Source synchrotron facility (Oxfordshire, UK). Protein samples at concentrations >5 mg/ml were loaded onto a Superdex™ 200 Increase 10/300 GL size exclusion chromatography column (GE Healthcare) in 20 mM Tris pH 8.0, 150 mM KCl at 0.5 ml/min using an Agilent 1200 HPLC system. The column elution passed through the experimental cell, with SAXS data recorded at 12.4 keV, detector distance 4.014 m, in 3.0 s frames. ScÅtter 3.0 (http://www.bioisis.net) was used to subtract, average the frames and carry out the Guinier analysis for the radius of gyration (*Rg*), and *P(r)* distributions were fitted using *PRIMUS*[42]. *Ab initio* modelling was performed using *DAMMIF*[43] imposing P1 or P2 symmetry (as indicated) and 30 independent runs were averaged and displayed as *DAMFILT* envelopes.

Yeast two-hybrid (Y2H)

Sequences corresponding to human SYCP1 (1-811, 101-783, 1-362, 101-362, 1-206) and SYCE3 (1-88) were cloned into pGBKT7 vectors (Clontech) and human sequences for SYCP1 (1-811), SYCE3 (1-88), SYCE1 (1-351), SYCE2 (1-218), TEX12 (1-123) and SIX6OS1 (1-587) were cloned into pGADT7 vectors (Clontech). The Matchmaker™ Gold system (Clontech) was used for Y2H analysis, using manufacturer's instructions. Yeast transformations were performed by the standard PEG/ssDNA/LiAc protocol, with the Y187 strain transformed with pGBKT7 vectors and Y2H Gold strain transformed with pGADT7 vectors. The two strains were mated in 0.5 ml 2xYPDA at 30°C, 50 r.p.m, by mixing

respective single colonies. Mated cultures were pelleted and resuspended in 0.5xYPDA for plating onto SD/-Trp/-Leu to select for mated colonies and also onto SD/-Trp/-Leu/-Ade/-His with X-α-gal to detect mated colonies that have activated the ADE1, HIS3 and MEL1 reporter genes. Plates were incubated for 5 days at 30°C before imaging.

Transmission electron microscopy (TEM)

TEM experiments were performed using a Philips CM100 TEM (Electron Microscopy Research services, Newcastle University). SYCE2-TEX12 samples at 3 mg/ml were incubated with a two-fold molar excess of SYCE3 and were applied to carbon-coated grids, washed and then negatively stained with 0.1% v/v uranyl acetate for imaging.

Protein structure analysis

Molecular structures images were generated using the PyMOL Molecular Graphics System, Version 2.4 Schrödinger, LLC.

CRISPR/Cas9 Gene Editing

Syce3 mutant mice were generated by Alt-R CRISPR[44] using a paired nickase design to minimise off-target mutations[45]. Guide RNA complexes were prepared by annealing 1:1 molar ratios of crRNA (oligos Syce3_20092 or Syce3_20053; Supplementary Table 1) and tracrRNA (IDT). CBAB6F1 female mice (Charles River) were superovulated with 5 IU pregnant mare serum followed by 5 IU human chorionic gonadotophin 42-48 hours later, then mated with CBAB6F1 males. Zygotes were isolated at E0.5 and Alt-R CRISPR reagents (20 ng/μL Alt-R S.p. Cas9 D10A nickase V3 (IDT), 10 ng/μL each guide RNA complex, 20 ng/μL total ssDNA repair oligo in 10 mM Tris pH 7.5, 0.1 mM EDTA) microinjected into the cytoplasm. Zygotes were cultured overnight in KSOM, then transferred to the oviduct of pseudopregnant recipient females. The resulting pups were genotyped from ear clips by sequencing the PCR products obtained using primers Syce3_O2F and Syce3_O2R (Supplementary Table 1). The WY repair oligo introduces W41E and Y41E amino acid mutations into *Syce3* and includes two silent mutations within the nickase PAM sites (Supplementary Table 1). The control PAM repair oligo only contains the two silent PAM site mutations. Adult F0 animals were culled by cervical dislocation and tissues dissected in PBS for analysis. For the silent PAM site mutations, two $Syce3^{PAM/PAM}$ homozygous animals were obtained directly from the CRISPR/Cas9 injections, additional homozygous animals were then generated by breeding. Matings with male or female mice carrying the $Syce3^{WY}$ allele were not productive.

Mouse Phenotyping

Adult mice were culled by cervical dislocation at 2-4 months old, and their testes and epididymides dissected in PBS. Testis weights and cauda epididymis sperm counts were obtained as described previously[46]. For testis histology, testes were fixed in Bouin's fixative, embedded in wax, sectioned, and stained with haematoxylin and eosin[46]. Although CRISPR/Cas9 founder animals can exhibit mosaicism[27,28], the mouse germline typically originates from only three or four epiblast cells[47,48], and we did not detect regions of phenotypic mosaicism in the testes of the animals selected for this study.

Meiotic Chromosome Spreads

Chromosome spreads were prepared from adult *Syce3* testes as described[49]. Chromosome spreads were stained with antibodies as described[29]. Primary antibodies were mouse anti-SYCP3 (Abcam #ab97672, 1:500), rabbit anti-SYCP1 (Abcam #ab15090, 1:200) and rabbit anti-RAD51 (Millipore #PC 130, 1:500). Slides were mounted using antifade mounting medium (Vectashield, H-1000) and high precision coverslips (Marienfeld).

Widefield Fluorescent Imaging

Widefield epifluorescent images were acquired for a single plane using a Zeiss Axioplan II fluorescence microscope with a Photometrics Coolsnap HQ2 CCD camera, and multiple z-planes using a Zeiss AxioImager M2 fluorescence microscope with a Photometrics Prime BSI CMOS camera. Image capture was performed using Micromanager (Version 1.4), z-stacks were deconvolved in Huygens Essential and maximum intensity projected, and all images were analysed in Fiji.

Super-Resolution Imaging

Three dimensional SIM images were captured with a Nikon N-SIM microscope with an Andor iXon 897 EMCCD camera (Andor technologies, Belfast UK). Consistent capture parameters were used for given antibody combinations. Chromosome spreads that extended beyond the field of view were captured as multiple images with 15% overlap (Extended Data Fig. 10), then stitched together using Nikon NIS-Elements. Maximum intensity projections were taken forward for further analysis. Custom pipelines in Fiji, Python and R were used to quantitatively analyse the SIM images.

Quantitative Image Analysis

Binary masks were generated in Fiji by manual thresholding of antibody-stained channels, and individual nuclear territories by drawing a region of interest around DAPI staining. Masks were converted into labelmaps for focal staining patterns. Downstream analysis was performed in Python3 and R.

Focal labels were shuffled within the nuclear territory by randomly assigning new centroid coordinates to each focus within the nuclear space, ensuring that the edges of each focus territory did not overlap one another or exceed the nuclear boundary. For calculation of mean fluorescence intensity within foci, the mean nuclear background signal from the area not assigned to foci was first subtracted to control for background variation.

Extended Data

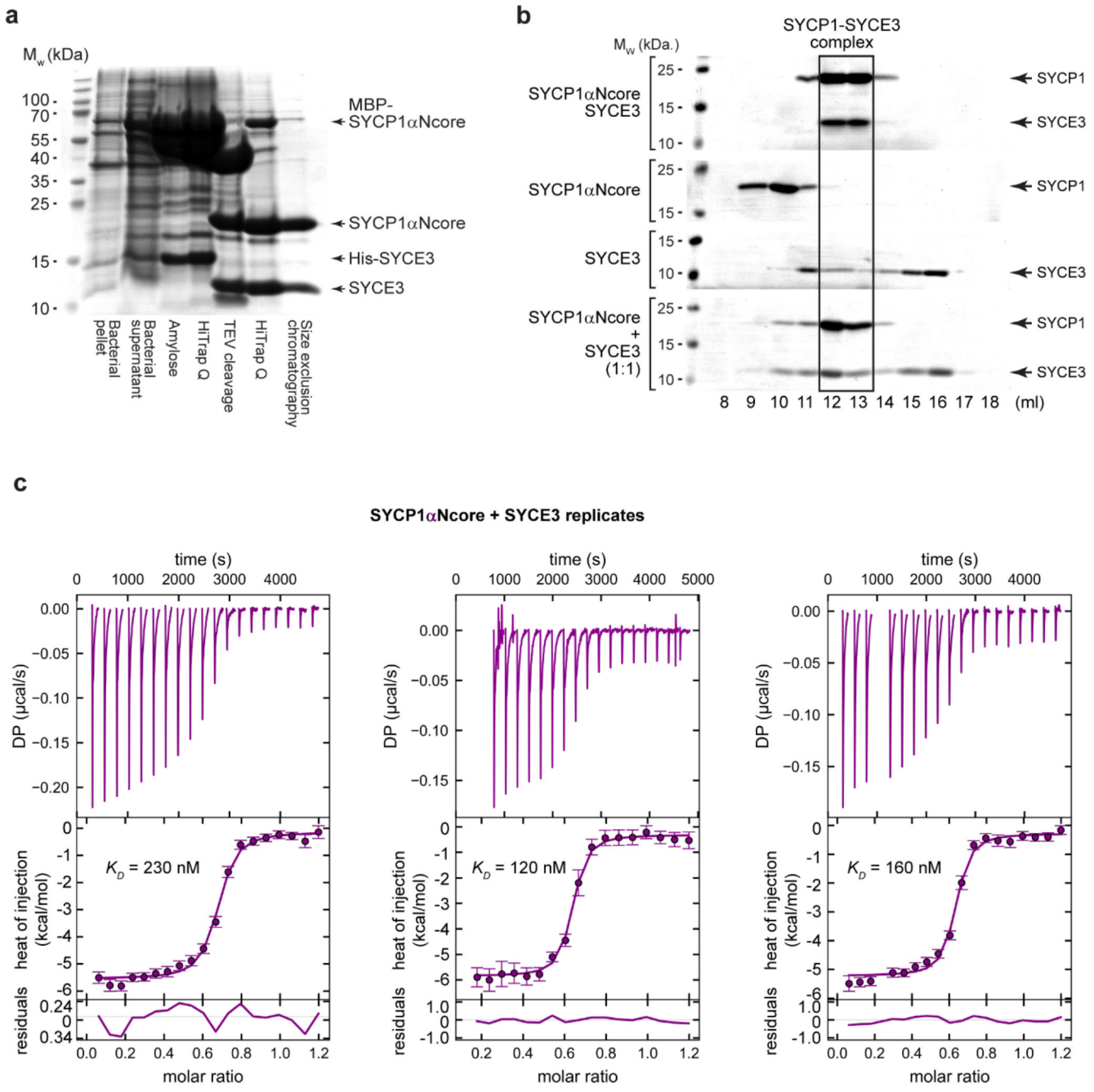

Extended Data Fig. 1. SYCP1 forms a high-affinity complex with SYCE3.

(**a**) Recombinant co-expression and co-purification of SYCP1αNcore-SYCE3 through amylose and anion exchange chromatography, followed by TEV cleavage to remove N-terminal expression tags, with subsequent anion exchange and size exclusion chromatography. (**b**) SDS-PAGE of elution fractions corresponding to the size-exclusion chromatography analysis shown in Fig. 1f. (**c**) Isothermal calorimetry (ITC) of SYCE3 titrated into SYCP1αNcore, demonstrating an apparent affinity of 170 ± 30 nM (mean ±

SEM, n=3 biologically independent replicates), corresponding to Fig. 1h. The injections (top), fit (middle) and residuals (bottom) are shown for the three biological replicates, with individually determined apparent affinities of 230 nM, 120 nM and 160 nM (the binding curve of the 160 nM replicate is shown in Fig. 1h.). Error bars correspond to the estimated error of each integrated isotherm based on baseline uncertainty (calculated in *NITPIC*).

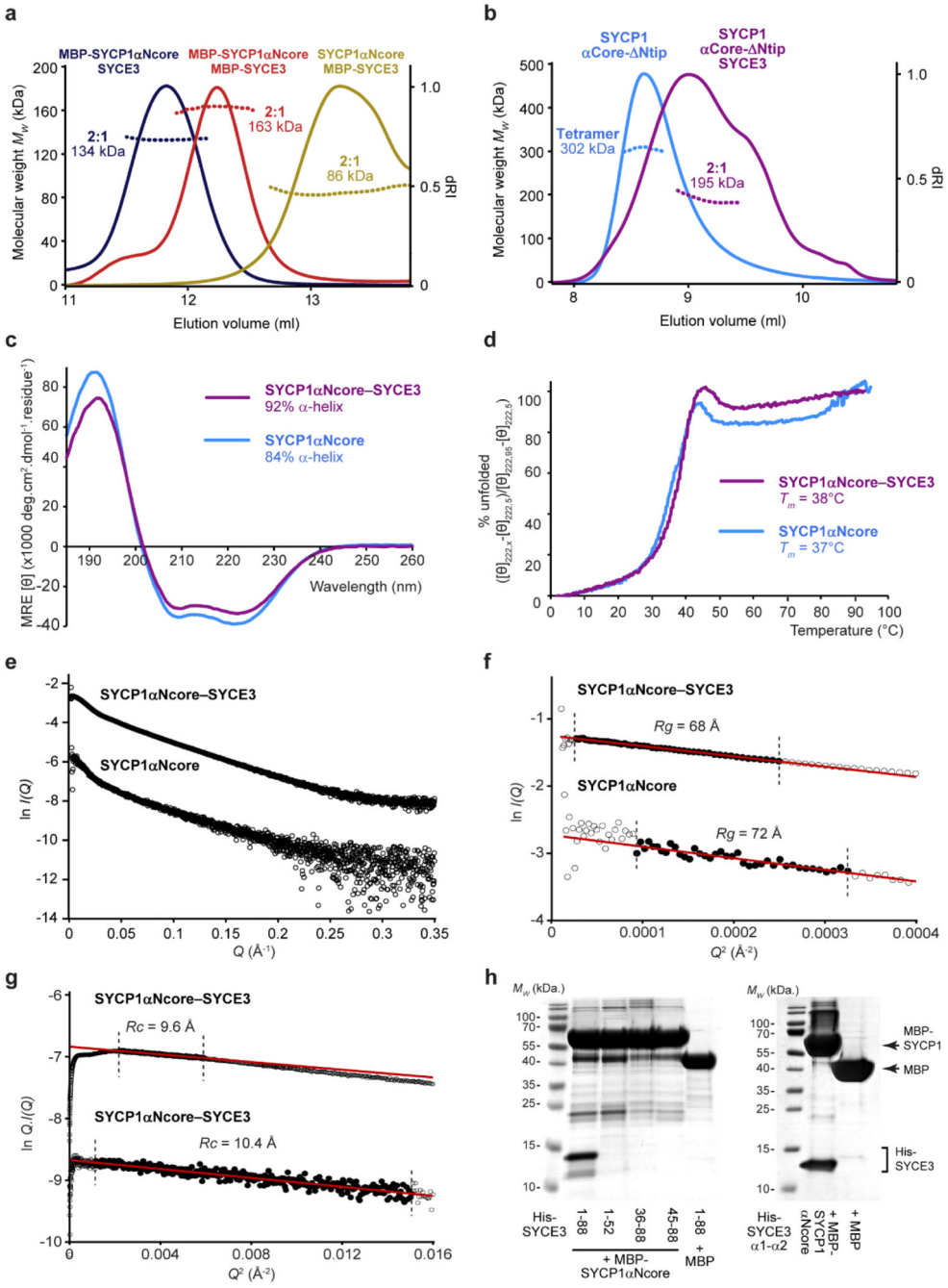

Extended Data Fig. 2. Structure of the SYCP1αNcore-SYCE3 complex.

Europe PMC Funders Author Manuscripts

(**a**) SEC-MALS analysis of MBP-SYCP1αNcore-SYCE3 (blue), MBP-SYCP1αNcore-MBP-SYCE3 (red), SYCP1αNcore-MBP-SYCE3 (yellow), revealing 2:1 complexes of 134 kDa, 163 kDa and 86 kDa, respectively (theoretical – 134 kDa, 175 kDa and 94 kDa). (**b**) SEC-MALS analysis of SYCP1 αCore-ΔNtip in isolation and in complex with SYCE3, demonstrating a 302 kDa tetramer and 195 kDa 2:1 complex, respectively (theoretical – 320 kDa and 171 kDa). (**c**) Far UV CD spectra and (**d**) CD thermal denaturation of SYCP1αNcore-SYCE3 (purple) and SYCP1αNcore (blue). (**c**) Secondary structure composition was estimated through deconvolution of spectra with data fitted at normalised rms deviation values of 0.006 and 0.001, respectively. (**d**) Thermal denaturation recorded for SYCP1αNcore-SYCE3 and SYCP1αNcore as % unfolded based on the helical signal at 222 nm; melting temperatures were estimated at 38°C and 37°C, respectively. (**e-g**) SEC-SAXS analysis. (**e**) Scattering intensity plots, (**f**) Guinier analysis to determine the radius of gyration (Rg) with linear fits shown in black (Q.Rg values were < 1.3) and (**g**) Guinier analysis to determine the radius of gyration of the cross-section (Rc) (Q.Rc values were < 1.3) for SYCP1αNcore-SYCE3 and SYCP1αNcore. Corresponding *P(r)* distributions and *ab initio* models are shown in Fig. 2b. (**h**) SYCE3-binding analysis through co-expression with MBP-SYCP1 or free MBP and co-purification by amylose, ion exchange and size-exclusion chromatography using SYCP1αNcore and SYCE3 truncations.

Europe PMC Funders Author Manuscripts

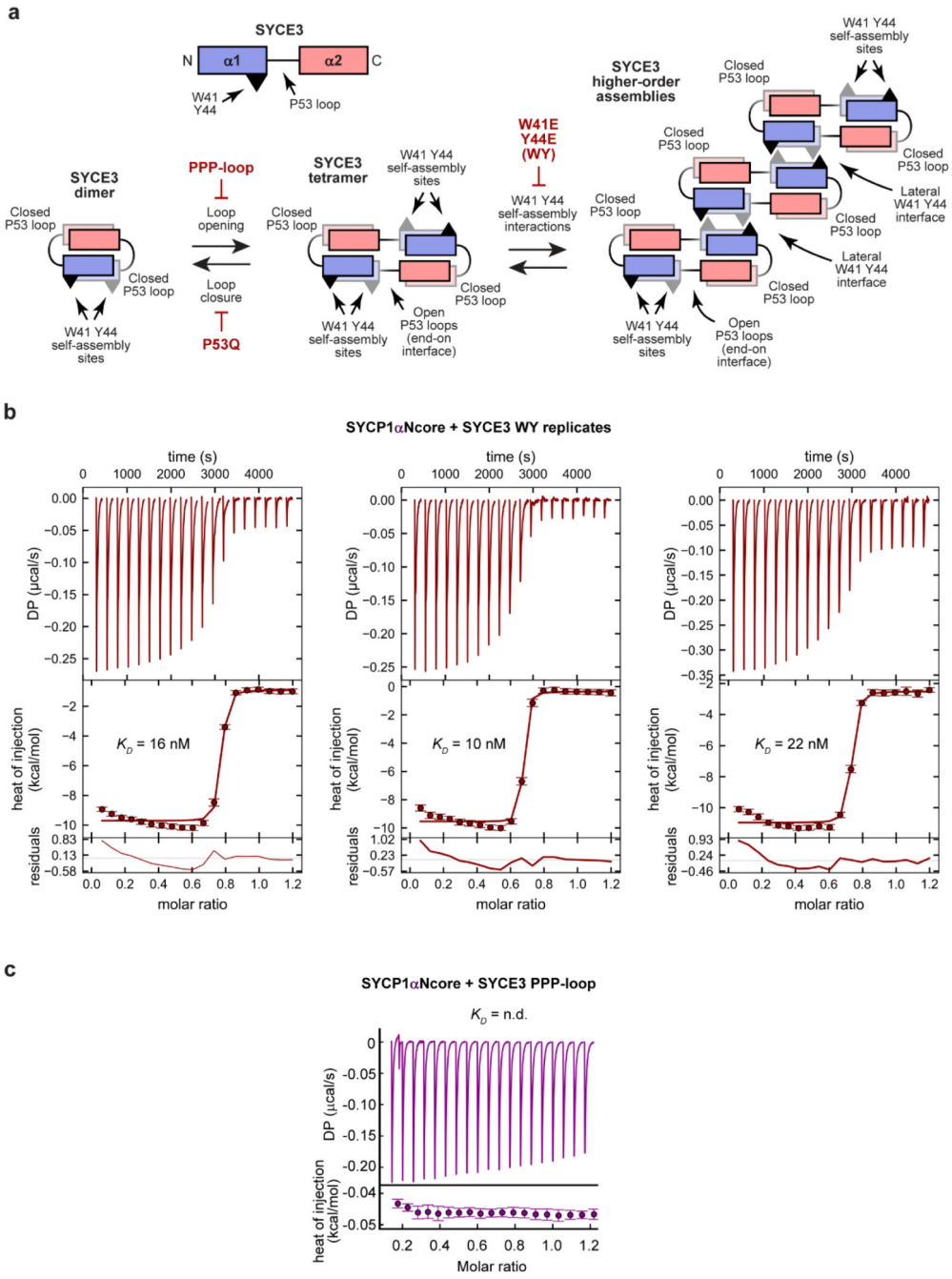

Extended Data Fig. 3. SYCP1 binds to the SYCE3 WY mutant.

(**a**) Schematic of the SYCE3 chain, dimeric structure and self-assembly into tetramers and higher-order structures. SYCE3 consists of two α-helices, α1 (blue) and α2 (red), which are linked together by the P53 loop. In the SYCE3 dimer, the P53 loop adopts a closed conformation. This structure self-assembles through one of its P53 loops opening, creating a tetramer consisting of two linear chains and two helix-loop-helix chains. SYCE3 tetramer formation is blocked by the PPP-loop mutation which supports the dimeric closed loop conformation, but is incompatible with the assembled open loop conformation.

Similarly, SYCE3 constitutively assembles upon P53Q mutation, which is incompatible with the closed loop conformation. SYCE3 tetramers undergo higher-order assembly through lateral interaction of their W41 Y44 sites. The resultant higher-order structures are held together by the combined actions of the end-on interface of the tetramer and the lateral interfaces mediated by W41 and Y44. Higher-order assembly through lateral interactions is blocked by the W41E Y44E (WY) mutation. (**b**) ITC analysis of SYCE3 WY titrated into SYCP1αNcore, demonstrating an apparent affinity of 16 ± 3 nM (mean ± SEM, n=3 biologically independent replicates), corresponding to Fig. 2g. The injections (top), fit (middle) and residuals (bottom) are shown for the three biological replicates, with individually determined apparent affinities of 16 nM, 10 nM and 22 nM (the binding curve of the 16 nM replicate is shown in Fig. 2g.). (**c**) ITC of SYCE3 PPP-loop titrated into SYCP1αNT, in which no interaction was not observed and the binding affinity was not determined (n.d.). (**b**,**c**) Error bars correspond to the estimated error of each integrated isotherm based on baseline uncertainty (calculated in *NITPIC*).

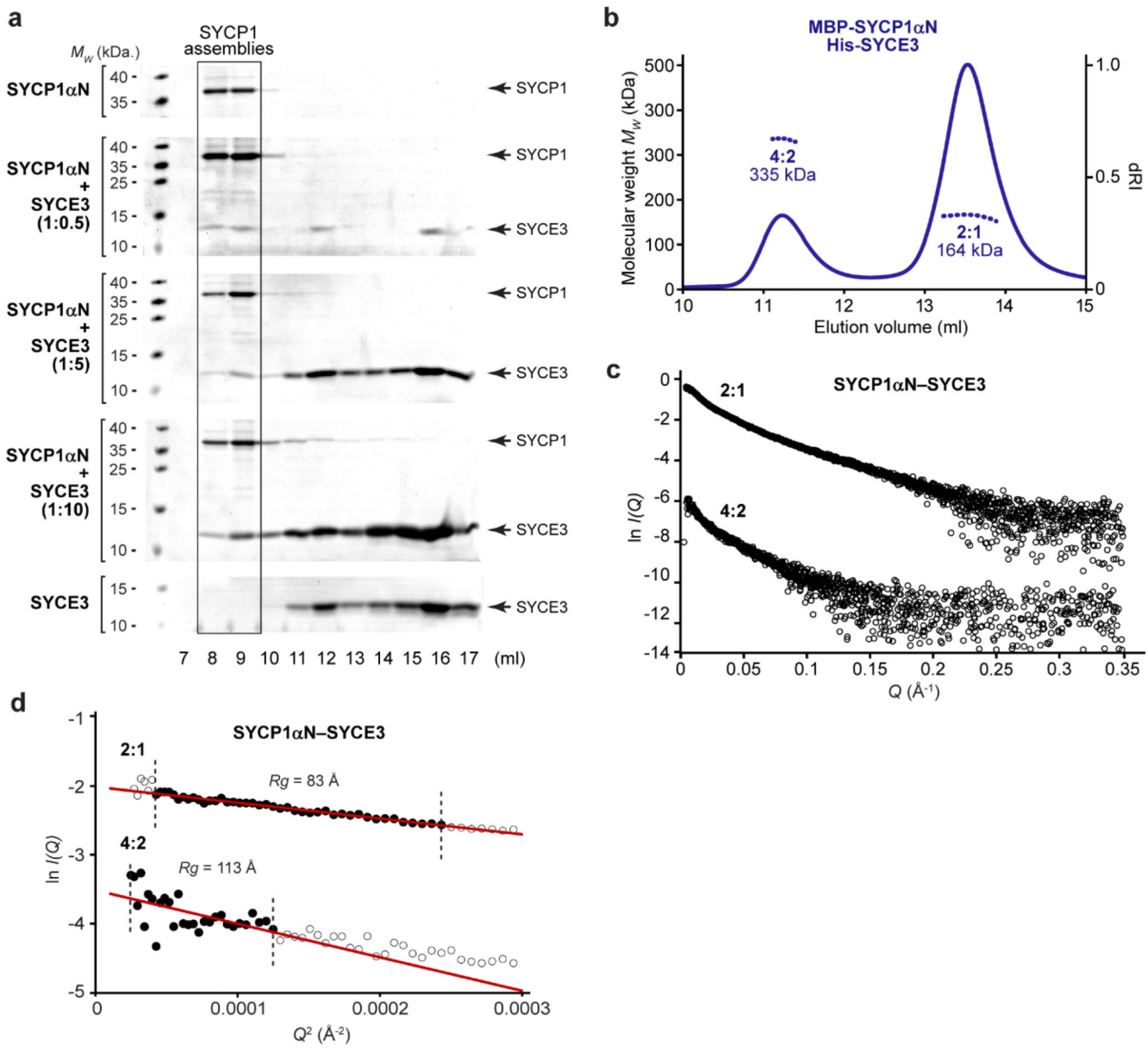

Extended Data Fig. 4. Structure of the SYCP1αN-SYCE3 complex.

(**a**) SDS-PAGE of size-exclusion chromatography elution fractions of 127 μM SYCP1αN upon incubation with SYCE3 at stoichiometric ratios (per molecule) of 1:0.5, 1:5 and 1:10; free SYCP1αN and SYCE3 are shown for comparison. (**b**) SEC-MALS analysis (using a Superose 6 increase 10/300 GL column) of MBP-SYCP1αN-His-SYCE3 revealing 2:1 and 4:2 species of 164 kDa and 335 kDa, respectively (theoretical – 160 kDa and 319 kDa). (**c,d**) SEC-SAXS analysis. (**c**) Scattering intensity plots and (**d**) Guinier analysis to determine the radius of gyration (Rg) with linear fits shown in black (Q.Rg values were < 1.3) for SYCP1αN-SYCE3 2:1 and 4:2 complexes. Corresponding *P(r)* distributions and *ab initio* models are shown in Fig. 3c,d.

Europe PMC Funders Author Manuscripts

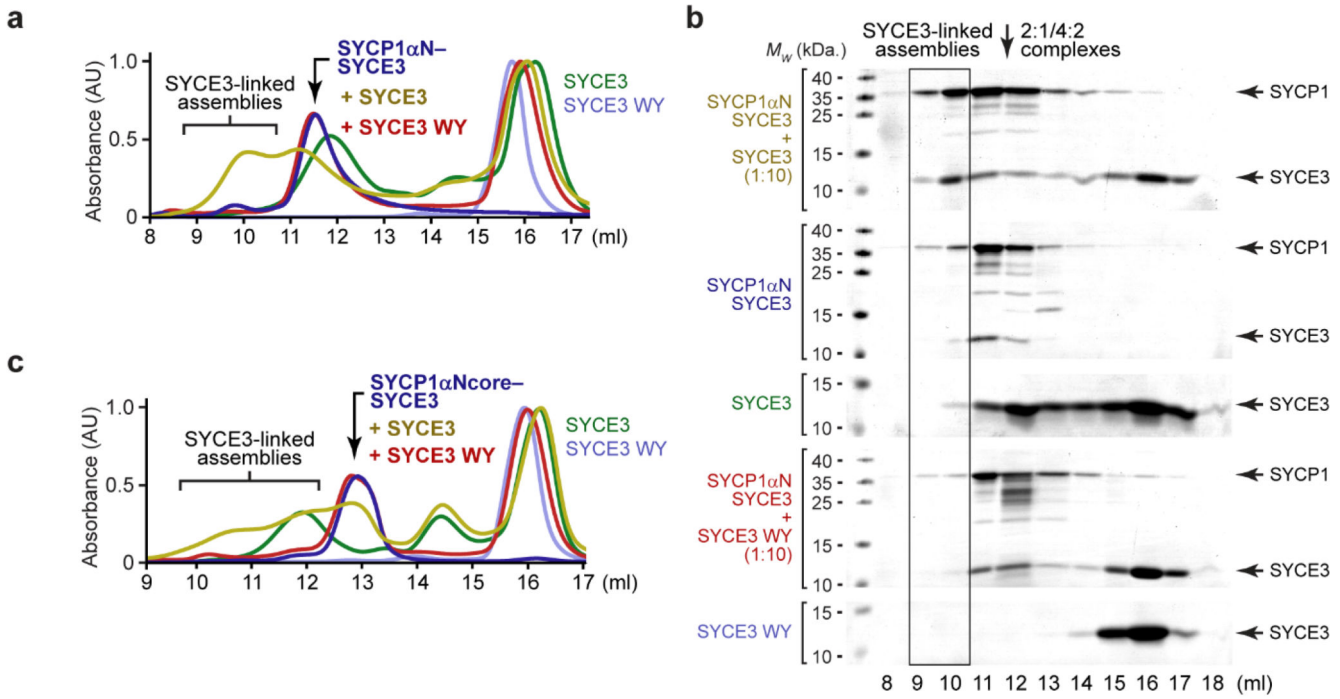

Extended Data Fig. 5. SYCP1-SYCE3 integrated lattice formation through SYCE3 self-assembly.

(**a**) Size-exclusion chromatography of (**a,b**) 95 μM SYCP1αN-SYCE3 and (**c**) 95 μM SYCP1αNcore-SYCE3 upon incubation with a 10-fold stoichiometric excess (per molecule) of SYCE3 wild-type or WY, corresponding to Fig. 4f-h. (**a,c**) UV absorbance (280 nm) chromatograms normalised to the same maximum peak height shown in Fig. 3f,g with additional chromatograms for free SYCE3 wild-type and WY.

Europe PMC Funders Author Manuscripts

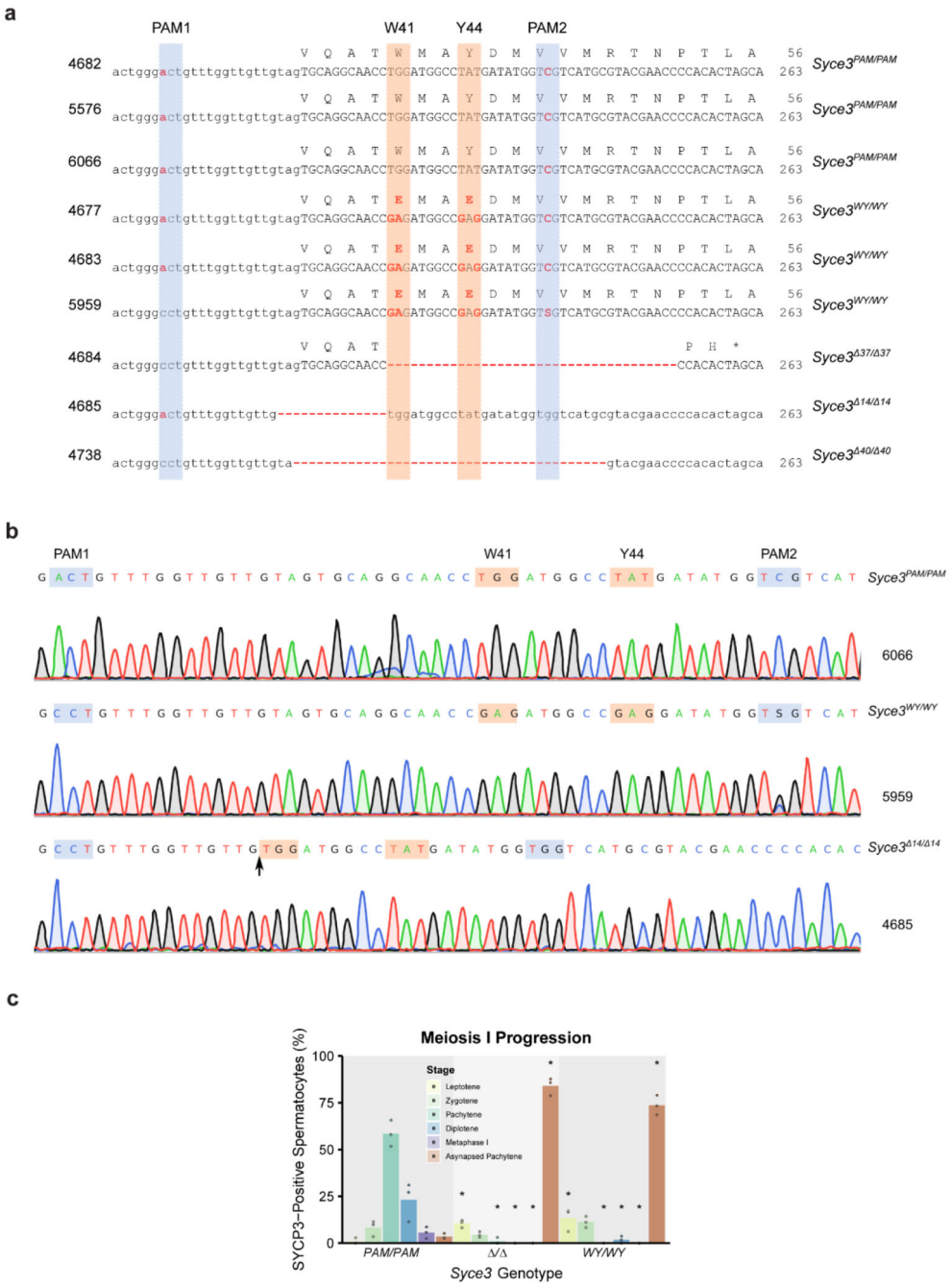

Extended Data Fig. 6. *Syce3* mutant allele sequences and meiotic phenotypes.

(**a**) *Syce3* nucleotide and predicted protein sequences of mice used in this study. Mouse IDs are shown on the left and the genotype group on the right. Animal 5959 in the $Syce3^{WY/WY}$ group did not incorporate the silent C:A mutation in PAM1 and was mosaic/heterozygous for the silent G:C mutation in PAM2. For the $Syce3^{\Delta/\Delta}$ group the number of nucleotides deleted is indicated in the allele name. The PAM sequences are highlighted with blue boxes, the W41 and Y44 sequences with orange boxes. (**b**) Chromatograms showing examples of sequencing the *Syce3* locus from mice with the indicated genotypes and IDs. Mice

Europe PMC Funders Author Manuscripts

that lacked potential mosaicism/heterogeneity at the W41/Y44 codons were used in this study. (**c**) Percentage of SYCP3-positive spermatocytes at the indicated stage of meiosis I in *Syce3* chromosome spreads based on SYCP3 and SYCP1 immunostaining (Fig. 4f). Mean percentages for each genotype are indicated by the bars, percentages from individual animals are indicated by filled circles. Asterisks indicate a significant difference ($p<0.05$, Student's t-test, n=3) relative to *Syce3*$^{PAM/PAM}$ controls.

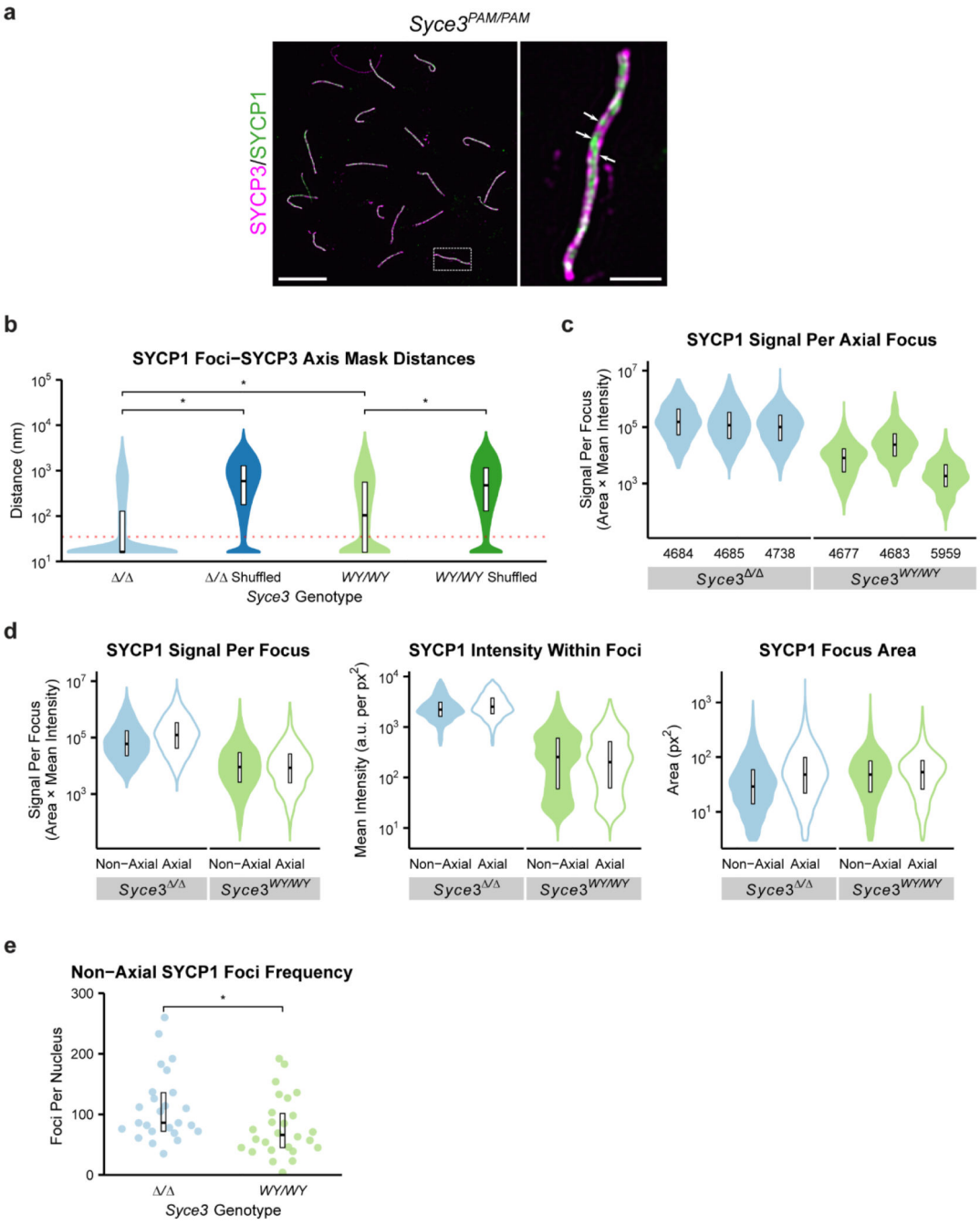

Extended Data Fig. 7. Quantitative analysis of SYCP1 foci in *Syce3* spermatocytes.

(**a**) SIM images of pachytene *Syce3*$^{PAM/PAM}$ meiotic chromosome spreads immunostained for SYCP3 (magenta) and SYCP1 (green). Scale bars, 10 μm for low magnification images, 1 μm for enlarged regions. Patches where SYCP1 extends linearly along one axis are indicated with arrows. The spread shown is the same as in Fig. 5a (**b**) SYCP1 foci-SYCE3 axis mask distances. Distances from the centroid of each SYCP1 focus to the nearest point on the SYCP3 axis mask are shown alongside distances from shuffled datasets obtained by assigning all SYCP1 foci in each nucleus to a random nuclear location for twenty iterations. The red dotted horizontal line represents the 35 nm threshold distinguishing axial and non-axial foci. Crossbars represent quartiles; *, $p< 0.01$ (Mann-Whitney U test, paired test used to compare observed with shuffled datasets, nuclei medians are 16, 603, 91 and 494 nm, n=25, 26 nuclei); 3 animals analysed for each *Syce3* genotype. (**c**) Total SYCP1 signal in each axial SYCP1 focus as shown in Fig. 5d, with data segmented for individual animals. Crossbars represent quartiles; medians are 152975, 116615, 101019, 8067, 24188 and 1855 arbitrary units); mouse IDs are shown below each dataset. (**d**) Violin plots showing the anti-SYCP1 immunostaining signal per focus, intensity within foci and focus area for axial and non-axial SYCP1 foci in *Syce3*$^{\Delta/\Delta}$ and *Syce3*$^{WY/WY}$ spermatocytes. Crossbars represent quartiles. Median SYCP1 signals per focus: 60101, 123441, 9061 and 8485 arbitrary units. Median SYCP1 intensities within foci; 2205, 2525, 255, and 203 arbitrary units per px^2. Median areas; 29, 48, 48 and 53 nm^2. 3 animals analysed for each *Syce3* genotype. (**e**) Non-axial SYCP1 foci frequencies in asynapsed pachytene *Syce3*$^{\Delta/\Delta}$ and *Syce3*$^{WY/WY}$ spermatocytes. *, $p< 0.05$ (Mann-Whitney U test, medians are 86 and 66 foci, n=25, 26 nuclei); 3 animals analysed for each *Syce3* genotype.

Europe PMC Funders Author Manuscripts

Europe PMC Funders Author Manuscripts

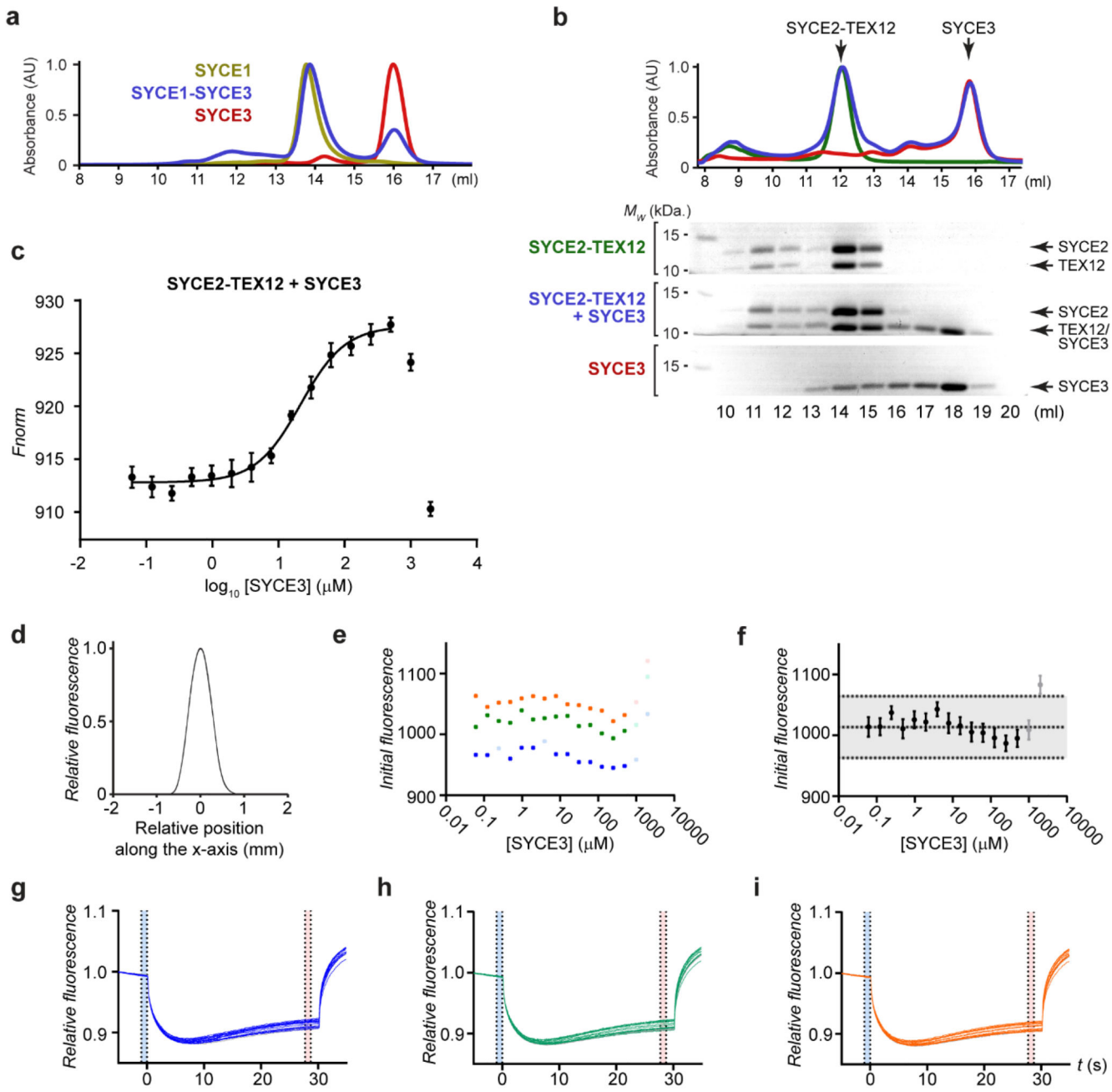

Extended Data Fig. 8. SYCE3 interacts with SYCE1-SIX6OS1 and SYCE2-TEX12 complexes.

(**a**) Size-exclusion chromatography of co-expressed and co-purified SYCE1core-SYCE3, with UV chromatograms of SYCE1core-SYCE3 (blue), SYCE1core (yellow) and SYCE3 (red), corresponding to Fig. 6e. (**b**) Size-exclusion chromatography of SYCE2-TEX12 core (green), SYCE3 (red) and an equimolar mixture of SYCE2-TEX12 core and SYCE3 (blue), shown as UV absorbance (280 nm). (**c-i**) MST analysis of SYCE3 titrated into 150 nM SYCE2-TEX12core, corresponding to Fig. 6f. (**c**) Full dataset in which the final two datapoints were excluded from analysis. The apparent binding affinity was determined to be 21.8 ± 2.1 μM (mean ± SEM,n=3 biologically independent replicates). (**d**) Overlaid capillary

scans. (**e,f**) Initial fluorescence for three data series (blue, yellow, green) displayed as (**e**) individual data series and (**f**) data represented as mean ± SEM (n=3 biologically independent replicates). (**g-i**) Relative fluorescence for each of the three data series.

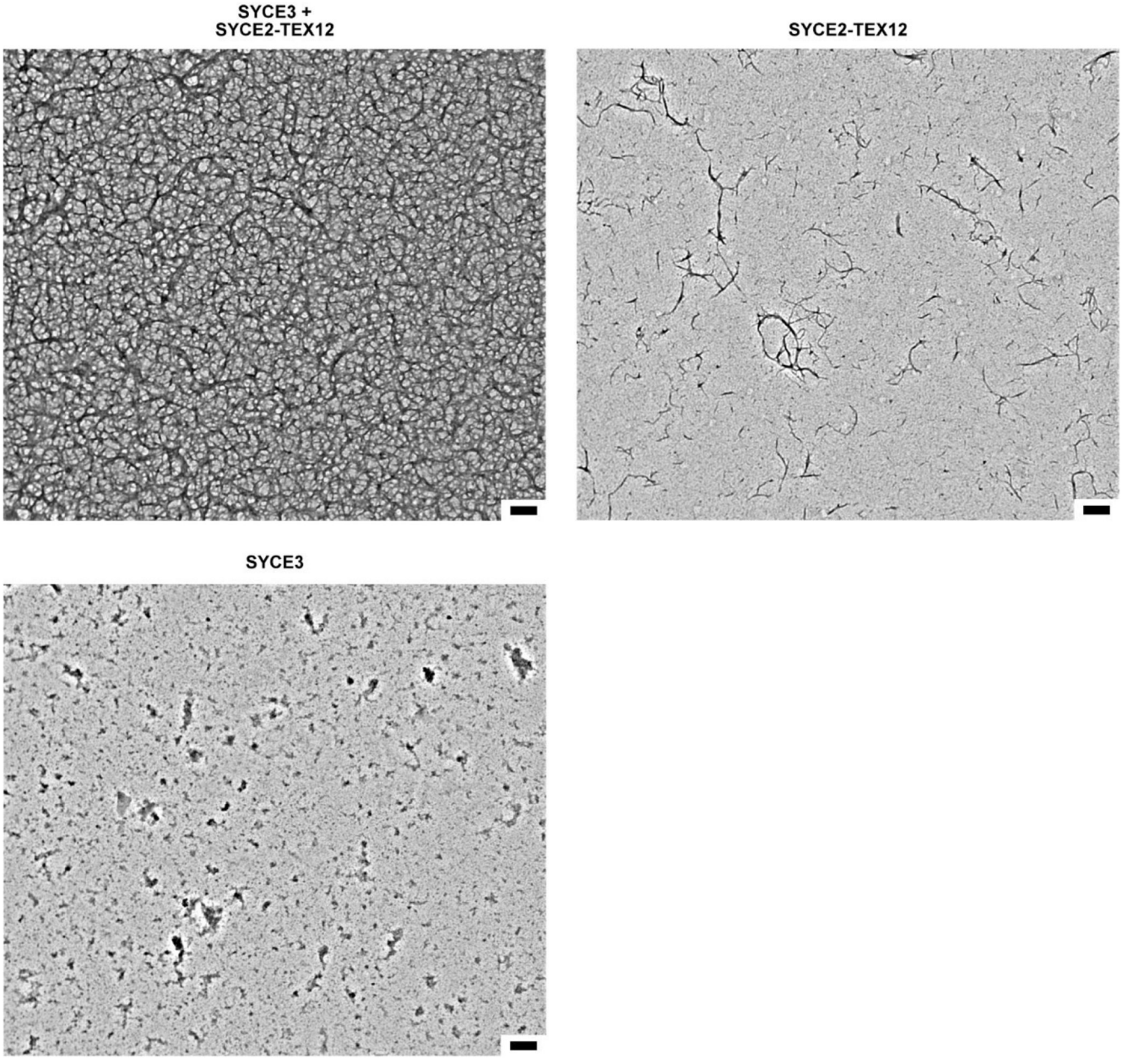

Extended Data Fig. 9. Electron microscopy analysis of SYCE2-TEX12 following incubation with a two-fold excess of SYCE3.

Full panels corresponding to Fig. 6g. Scale bar, 200 nm.

Europe PMC Funders Author Manuscripts

Europe PMC Funders Author Manuscripts

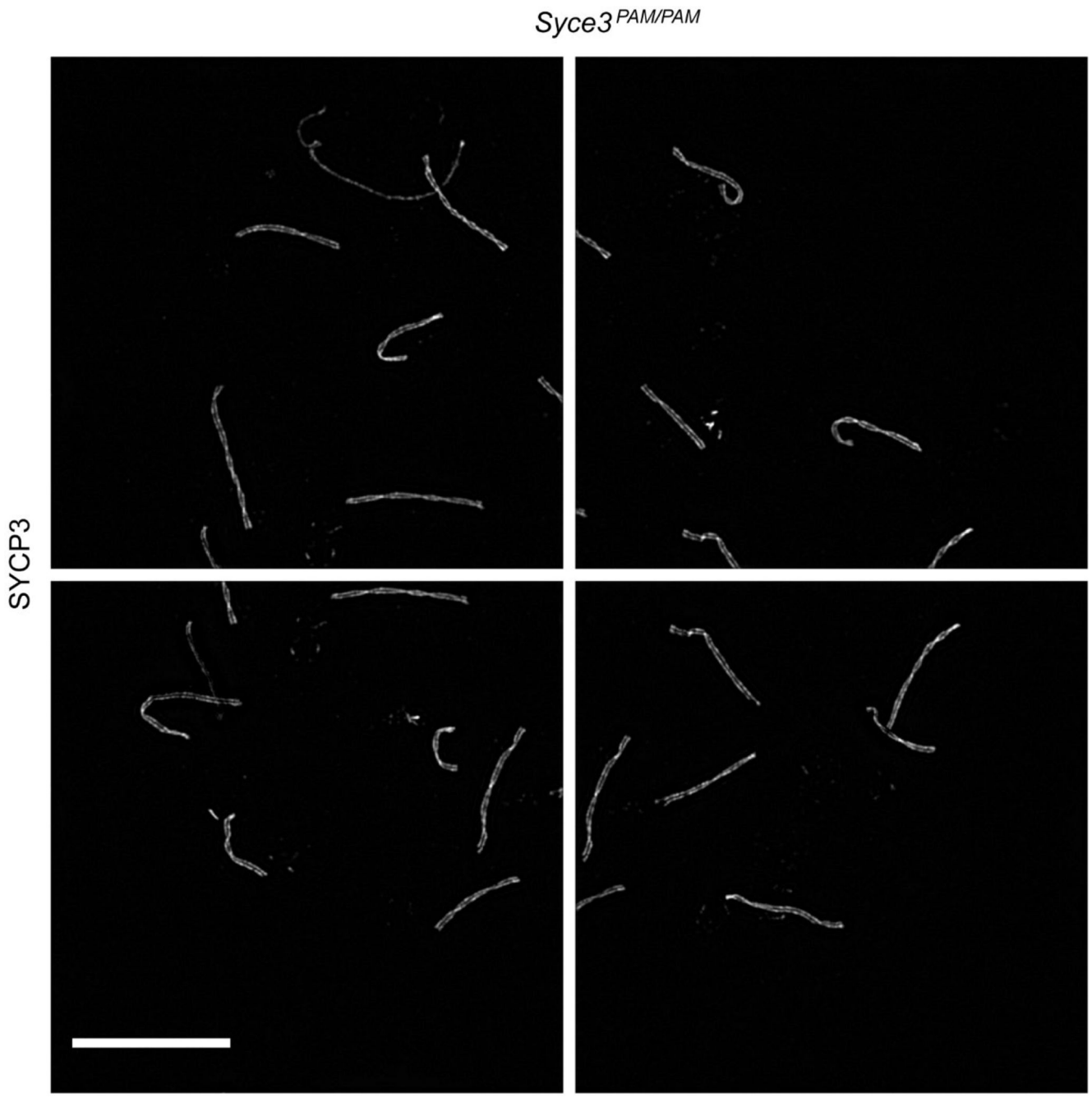

Extended Data Fig. 10. Overlapping images used to capture chromosome spreads.
Syce3$^{PAM/PAM}$ images used to capture the chromosome spread shown in Fig. 5b and Extended Data Fig. 7a. Scale bar, 10 μm. Overlapping images were taken with 15% overlap and stitched using algorithms in Nikon NIS-Elements.

Supplementary Material

Refer to Web version on PubMed Central for supplementary material.

Acknowledgements

We thank Diamond Light Source and the staff of beamline B21 (proposals sm14435, sm15580, sm15897 and sm15836). We thank H. Waller for assistance with CD data collection, and V. A. Jatikusumo and M. Ratcliff for work in the early stages of this project. We thank A. Wheeler, M. Pearson and L. Murphy in the MRC HGU advanced imaging resource for help and guidance with imaging and image analysis, the Edinburgh Super-Resolution Imaging Consortium for super-resolution imaging, and the University of Edinburgh Bioresearch & Veterinary Services for mouse husbandry. We thank Wendy Bickmore, Javier Caceres, Cova Vara and Adele Marston for critically reviewing the manuscript. This study was supported by MRC University Unit grant MC_UU_00007/6 (I.R.A. and J.H.C.) and a Wellcome Senior Research Fellowship (Grant Number 219413/Z/19/Z) (O.R.D.).

Data availability

This study used the publicly available dataset PDB accession number 6H86. The underlying data and uncropped gels corresponding to graphs and cropped gels in Figs. 1–6, and Extended Data Figs. 1, 3, 4, 5, 6, 7 and 8 are provided in Source Data files..

References

1. Hunter N. Meiotic Recombination: The Essence of Heredity. Cold Spring Harb Perspect Biol. 2015; 7
2. Zickler D, Kleckner N. Recombination, Pairing, and Synapsis of Homologs during Meiosis. Cold Spring Harb Perspect Biol. 2015; 7
3. Romanienko PJ, Camerini-Otero RD. The mouse Spo11 gene is required for meiotic chromosome synapsis. Mol Cell. 2000; 6: 975–87.
4. Geisinger A, Benavente R. Mutations in Genes Coding for Synaptonemal Complex Proteins and Their Impact on Human Fertility. Cytogenet Genome Res. 2016; 150: 77–85. [PubMed: 27997882]
5. Fan S, et al. Homozygous mutations in C14orf39/SIX6OS1 cause non-obstructive azoospermia and premature ovarian insufficiency in humans. Am J Hum Genet. 2021; 108: 324–336. [PubMed: 33508233]
6. Schilit SLP, et al. SYCP2 Translocation-Mediated Dysregulation and Frameshift Variants Cause Human Male Infertility. Am J Hum Genet. 2020; 106: 41–57. [PubMed: 31866047]
7. Solari AJ. Synaptosomal complexes and associated structures in microspread human spermatocytes. Chromosoma. 1980; 81: 315–37. [PubMed: 7192619]
8. Cahoon CK, Hawley RS. Regulating the construction and demolition of the synaptonemal complex. Nat Struct Mol Biol. 2016; 23: 369–77. [PubMed: 27142324]
9. Fraune J, Schramm S, Alsheimer M, Benavente R. The mammalian synaptonemal complex: Protein components, assembly and role in meiotic recombination. Exp Cell Res. 2012.
10. de Vries FA, et al. Mouse Sycp1 functions in synaptonemal complex assembly, meiotic recombination, and XY body formation. Genes Dev. 2005; 19: 1376–89. [PubMed: 15937223]
11. Schucker K, Holm T, Franke C, Sauer M, Benavente R. Elucidation of synaptonemal complex organization by super-resolution imaging with isotropic resolution. Proc Natl Acad Sci U S A. 2015; 112: 2029–33. [PubMed: 25646409]
12. Hamer G, et al. Characterization of a novel meiosis-specific protein within the central element of the synaptonemal complex. Journal of Cell Science. 2006; 119: 4025–4032. [PubMed: 16968740]
13. Hamer G, et al. Progression of meiotic recombination requires structural maturation of the central element of the synaptonemal complex. J Cell Sci. 2008; 121: 2445–51. [PubMed: 18611960]
14. Schramm S, et al. A novel mouse synaptonemal complex protein is essential for loading of central element proteins, recombination, and fertility. PLoS Genet. 2011; 7 e1002088 [PubMed: 21637789]
15. Gomez HL, et al. C14ORF39/SIX6OS1 is a constituent of the synaptonemal complex and is essential for mouse fertility. Nat Commun. 2016; 7 13298 [PubMed: 27796301]

16. Bolcun-Filas E, et al. SYCE2 is required for synaptonemal complex assembly, double strand break repair, and homologous recombination. Journal of Cell Biology. 2007; 176: 741–747. [PubMed: 17339376]
17. Bolcun-Filas E, et al. Mutation of the mouse Syce1 gene disrupts synapsis and suggests a link between synaptonemal complex structural components and DNA repair. PLoS Genet. 2009; 5 e1000393 [PubMed: 19247432]
18. Dunce JM, et al. Structural basis of meiotic chromosome synapsis through SYCP1 self-assembly. Nat Struct Mol Biol. 2018; 25: 557–569. [PubMed: 29915389]
19. Dunne OM, Davies OR. Molecular structure of human synaptonemal complex protein SYCE1. Chromosoma. 2019.
20. Dunne OM, Davies OR. A molecular model for self-assembly of the synaptonemal complex protein SYCE3. J Biol Chem. 2019; 294: 9260–9275. [PubMed: 31023827]
21. Sanchez-Saez F, et al. Meiotic chromosome synapsis depends on multivalent SYCE1-SIX6OS1 interactions that are disrupted in cases of human infertility. Sci Adv. 2020; 6
22. Syrjanen JL, Pellegrini L, Davies OR. A molecular model for the role of SYCP3 in meiotic chromosome organisation. Elife. 2014; 3
23. Dunce JM, Salmon LJ, Davies OR. Structural basis of meiotic chromosome synaptic elongation through hierarchical fibrous assembly of SYCE2-TEX12. Nat Struct Mol Biol. 2021; 28: 681–693. [PubMed: 34373646]
24. Ollinger R, Alsheimer M, Benavente R. Mammalian protein SCP1 forms synaptonemal complex-like structures in the absence of meiotic chromosomes. Mol Biol Cell. 2005; 16: 212–7. [PubMed: 15496453]
25. Hernandez-Hernandez A, et al. The central element of the synaptonemal complex in mice is organized as a bilayered junction structure. J Cell Sci. 2016; 129: 2239–49. [PubMed: 27103161]
26. Lu J, et al. Structural insight into the central element assembly of the synaptonemal complex. Sci Rep. 2014; 4 7059 [PubMed: 25394919]
27. Teboul L, Murray SA, Nolan PM. Phenotyping first-generation genome editing mutants: a new standard? Mamm Genome. 2017; 28: 377–382. [PubMed: 28756587]
28. Wang H, et al. One-step generation of mice carrying mutations in multiple genes by CRISPR/Cas-mediated genome engineering. Cell. 2013; 153: 910–8. [PubMed: 23643243]
29. Crichton JH, et al. Tex19.1 promotes Spo11-dependent meiotic recombination in mouse spermatocytes. PLoS Genet. 2017; 13 e1006904 [PubMed: 28708824]
30. Lizatovic R, et al. A De Novo Designed Coiled-Coil Peptide with a Reversible pH-Induced Oligomerization Switch. Structure. 2016; 24: 946–55. [PubMed: 27161978]
31. Roder K, Wales DJ. Transforming the Energy Landscape of a Coiled-Coil Peptide via Point Mutations. J Chem Theory Comput. 2017; 13: 1468–1477. [PubMed: 28177620]
32. Croasdale R, et al. An undecided coiled coil: the leucine zipper of Nek2 kinase exhibits atypical conformational exchange dynamics. J Biol Chem. 2011; 286: 27537–47. [PubMed: 21669869]
33. Jordan PW, Karppinen J, Handel MA. Polo-like kinase is required for synaptonemal complex disassembly and phosphorylation in mouse spermatocytes. J Cell Sci. 2012; 125: 5061–72. [PubMed: 22854038]
34. Spindler MC, Filbeck S, Stigloher C, Benavente R. Quantitative basis of meiotic chromosome synapsis analyzed by electron tomography. Sci Rep. 2019; 9 16102 [PubMed: 31695079]
35. Libuda DE, Uzawa S, Meyer BJ, Villeneuve AM. Meiotic chromosome structures constrain and respond to designation of crossover sites. Nature. 2013; 502: 703–6. [PubMed: 24107990]
36. Woglar A, Villeneuve AM. Dynamic Architecture of DNA Repair Complexes and the Synaptonemal Complex at Sites of Meiotic Recombination. Cell. 2018; 173: 1678–1691. e16 [PubMed: 29754818]
37. Pancsa R, Schad E, Tantos A, Tompa P. Emergent functions of proteins in non-stoichiometric supramolecular assemblies. Biochim Biophys Acta Proteins Proteom. 2019; 1867: 970–979. [PubMed: 30826453]

38. Davies OR, Maman JD, Pellegrini L. Structural analysis of the human SYCE2–TEX12 complex provides molecular insights into synaptonemal complex assembly. Open Biology. 2012; 2 120099 [PubMed: 22870393]
39. Keller S, et al. High-precision isothermal titration calorimetry with automated peak-shape analysis. Anal Chem. 2012; 84: 5066–73. [PubMed: 22530732]
40. Zhao H, Piszczek G, Schuck P. SEDPHAT--a platform for global ITC analysis and global multi-method analysis of molecular interactions. Methods. 2015; 76: 137–148. [PubMed: 25477226]
41. Brautigam CA, Zhao H, Vargas C, Keller S, Schuck P. Integration and global analysis of isothermal titration calorimetry data for studying macromolecular interactions. Nat Protoc. 2016; 11: 882–94. [PubMed: 27055097]
42. Konarev PV, Sokolova VVVAV, Koch MHJ, Svergun DI. PRIMUS - a Windows-PC based system for small-angle scattering data analysis. J Appl Cryst. 2003; 36: 1277–1282.
43. Franke D, Svergun DI. DAMMIF, a program for rapid ab-initio shape determination in small-angle scattering. J Appl Crystallogr. 2009; 42: 342–346. [PubMed: 27630371]
44. Quadros RM, et al. Easi-CRISPR: a robust method for one-step generation of mice carrying conditional and insertion alleles using long ssDNA donors and CRISPR ribonucleoproteins. Genome Biol. 2017; 18: 92. [PubMed: 28511701]
45. Shen B, et al. Efficient genome modification by CRISPR-Cas9 nickase with minimal off-target effects. Nat Methods. 2014; 11: 399–402. [PubMed: 24584192]
46. Ollinger R, et al. Deletion of the pluripotency-associated Tex19.1 gene causes activation of endogenous retroviruses and defective spermatogenesis in mice. PLoS Genet. 2008; 4 e1000199 [PubMed: 18802469]
47. Soriano P, Jaenisch R. Retroviruses as probes for mammalian development: allocation of cells to the somatic and germ cell lineages. Cell. 1986; 46: 19–29. [PubMed: 3013418]
48. Ueno H, Turnbull BB, Weissman IL. Two-step oligoclonal development of male germ cells. Proc Natl Acad Sci U S A. 2009; 106: 175–80. [PubMed: 19098099]
49. Costa Y, et al. Two novel proteins recruited by synaptonemal complex protein 1 (SYCP1) are at the centre of meiosis. J Cell Sci. 2005; 118: 2755–62. [PubMed: 15944401]

Europe PMC Funders Author Manuscripts

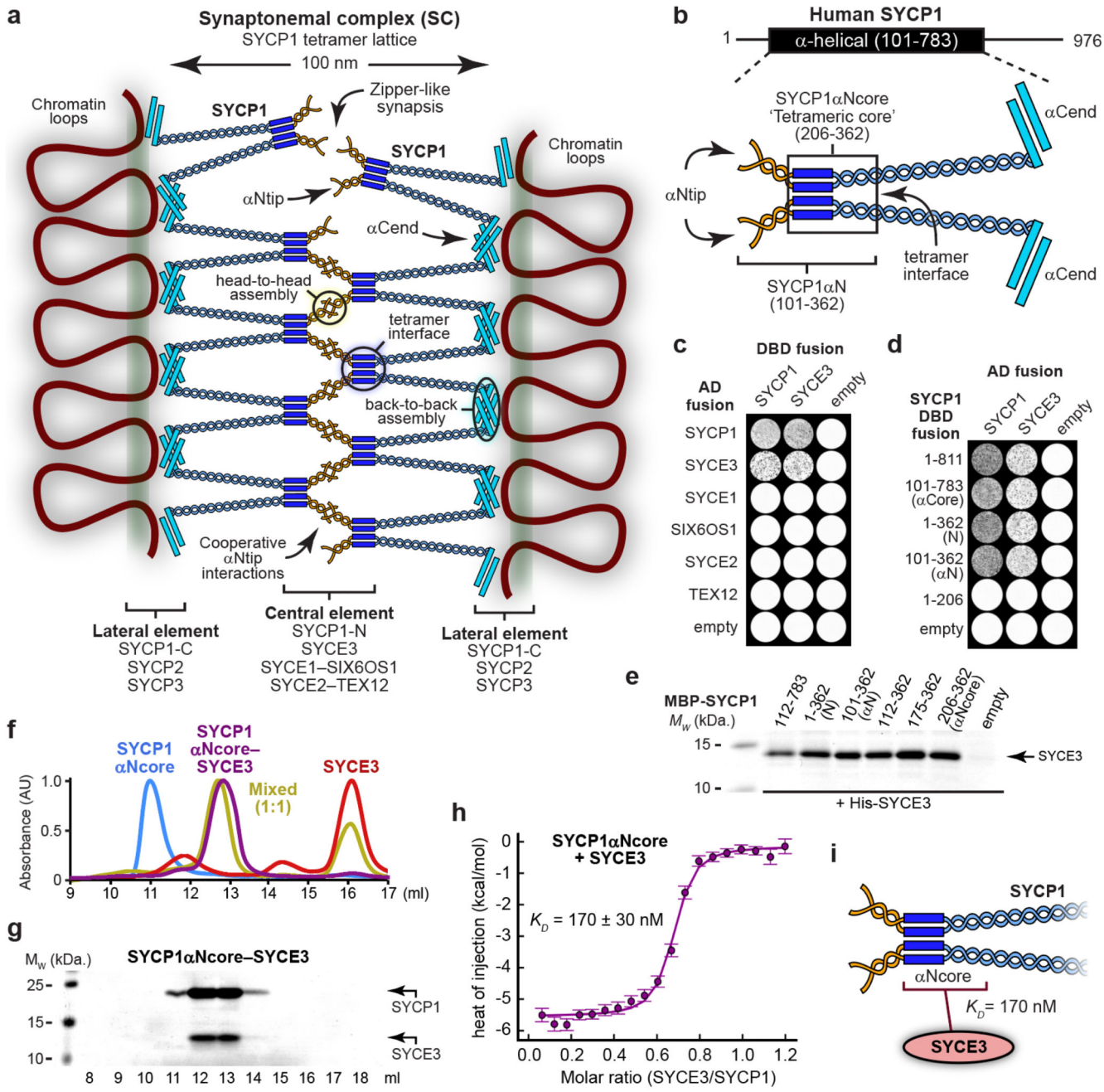

Fig. 1. SYCP1 interacts with central element protein SYCE3.

(**a**) Mammalian SC structure is defined by a supramolecular SYCP1 tetramer lattice, in which tetramer interfaces bind together parallel SYCP1 dimers and support cooperative head-to-head interactions between αNtip sites of bioriented SYCP1 tetramers, which are anchored to chromosome axes through back-to-back assembly of their α-helical C-termini[18]. (**b**) Schematic of SYCP1's α-helical core (amino-acids 101-783), highlighting its αNtip, αCend and tetramer interface. SYCP1αNcore (amino-acids 206-362; boxed) corresponds to the tetrameric core, whereas SYCP1αN (amino-acids 101-362) is extended to include αNtips that mediate higher-order assembly. (**c,d**) Yeast two-hybrid (Y2H) analysis of

(**c**) SYCP1 and SYCE3 interactions with SC proteins, and (**d**) SYCE3 interactions with truncated SYCP1 constructs. (**e**) Amylose pull-downs of SYCE3 following recombinant co-expression with MBP-SYCP1 constructs and free MBP (empty). (**f,g**) Size-exclusion chromatography of 235 μM SYCP1αNcore (blue), SYCE3 (red), SYCP1αNcore-SYCE3 (purple) and an equimolar mixture (per chain) of 235 μM SYCP1αNcore and SYCE3 (yellow), shown as (**f**) UV absorbance (280 nm) chromatograms normalised to the same maximum peak height and (**g**) SDS-PAGE of SYCP1αNcore-SYCE3 elution fractions; all elution profiles are shown in Extended Data Fig. 1b. (**h**) Isothermal calorimetry (ITC) of SYCE3 titrated into SYCP1αNcore, demonstrating an apparent affinity of 170 ± 30 nM (mean ± SEM, n=3 biologically independent replicates). The binding curve of one representative replicate is shown in which error bars correspond to the estimated error of each integrated isotherm based on baseline uncertainty (calculated in *NITPIC*). Full data of all three replicates are shown in Extended Data Fig. 1c. (**i**) Schematic illustrating that SYCE3 binds with nanomolar affinity (K_D = 170 nM) to SYCP1's tetrameric core.

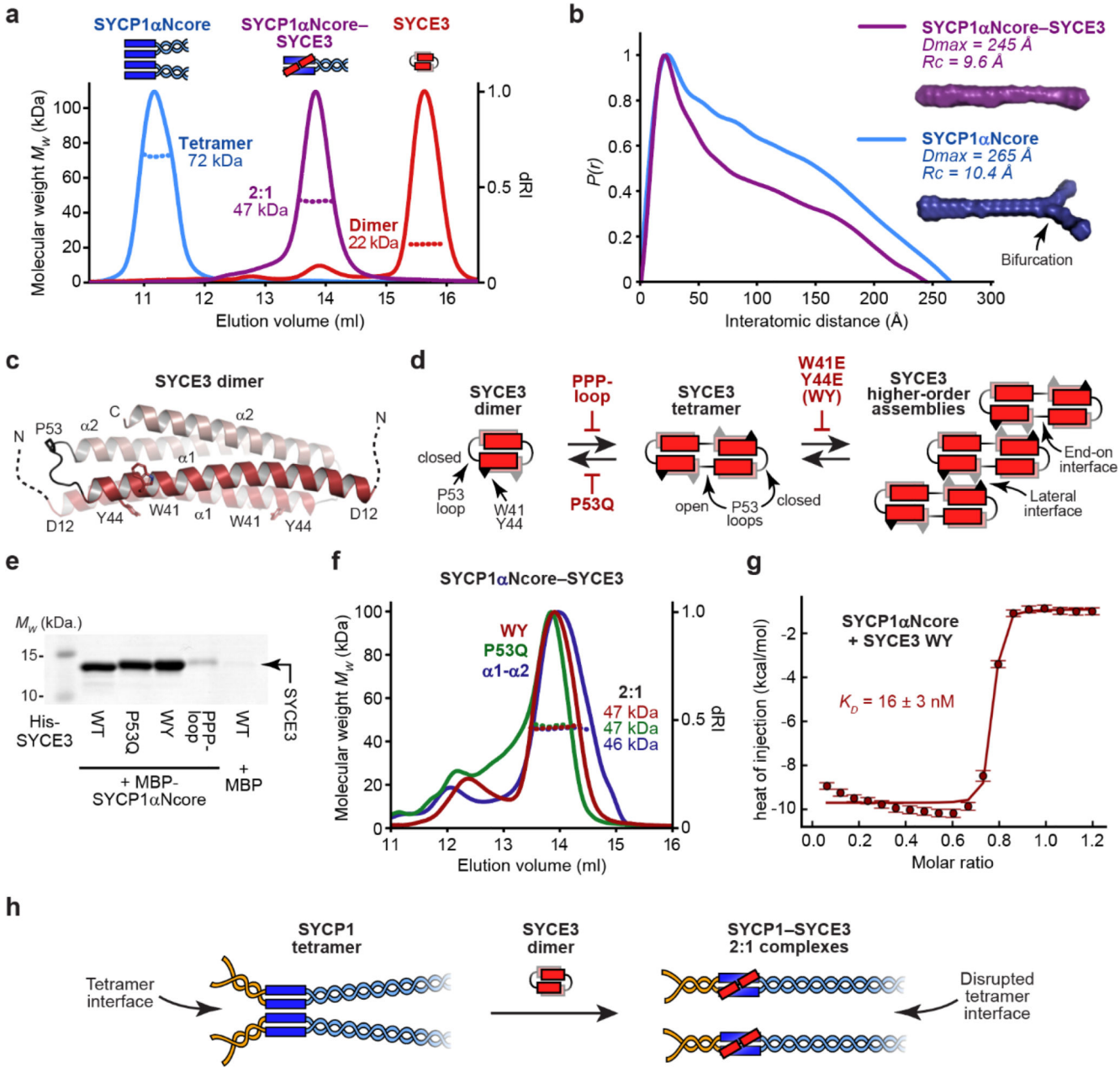

Fig. 2. SYCP1's tetramer interface is disrupted upon 2:1 complex formation with SYCE3

(**a**) SEC-MALS analysis showing differential refractive index (dRI; solid lines) profiles with fitted molecular weights (*Mw*; dashed lines) across elution peaks. SYCP1αNcore is a 72 kDa tetramer (blue), SYCE3 is a 22 kDa dimer (red) and SYCP1αNcore-SYCE3 is a 47 kDa 2:1 complex (purple); theoretical – 76 kDa, 21 kDa and 49 kDa. (**b**) SEC-SAXS *P(r)* distributions of SYCP1αNcore (blue) and SYCP1αNcore-SYCE3 (purple); maximum dimensions (*Dmax*) and cross-sectional radii (*Rc*) are shown alongside *ab initio* models. (**c**) Crystal structure of the SYCE3 dimer (pdb accession 6H86[20,26]), in which two helix-loop-helix chains (consisting of α1 and α2 helices) are interlaced in a four-helical bundle; amino-acids W41 and Y44, and the closed P53 loop are highlighted. (**d**) SYCE3 self-assembles

into an end-on tetramer by P53 loop-opening (promoted by P53Q and inhibited by PPP-loop mutations), and into higher-order species through W41/Y44 lateral interactions (inhibited by W41E Y44E mutation; herein referred to as WY)[20]. A more detailed schematic of SYCE3 self-assembly is show in Extended Data Fig. 3a. (**e**) SYCE3-binding by SYCP1 following co-expression and purification by amylose, ion exchange and size-exclusion chromatography, for MBP-SYCP1αNcore with SYCE3 point-mutations. (**f**) SEC-MALS analysis showing that SYCP1αNcore forms 2:1 complexes of 47 kDa, 48 kDa and 46 kDa with SYCE3 WY, P53Q and α1-α2 (amino-acids 12-88); theoretical – 49 kDa. (**g**) ITC of SYCE3 WY titrated into SYCP1αNcore, demonstrating an apparent affinity of 16 ± 3 nM (mean ± SEM, n=3 biologically independent replicates). The binding curve of one representative replicate is shown in which error bars correspond to the estimated error of each integrated isotherm based on baseline uncertainty (calculated in *NITPIC*). Full data of all three replicates are shown in Extended Data Fig. 3b. (**h**) Schematic of SYCP1-SYCE3 2:1 complex formation. SYCP1 tetramers and SYCE3 dimers undergo conformational change, in which SYCE3 chains adopt extended open-loop conformations that bind to SYCP1 dimers, competitively inhibiting SYCP1's tetramer interface.

Europe PMC Funders Author Manuscripts

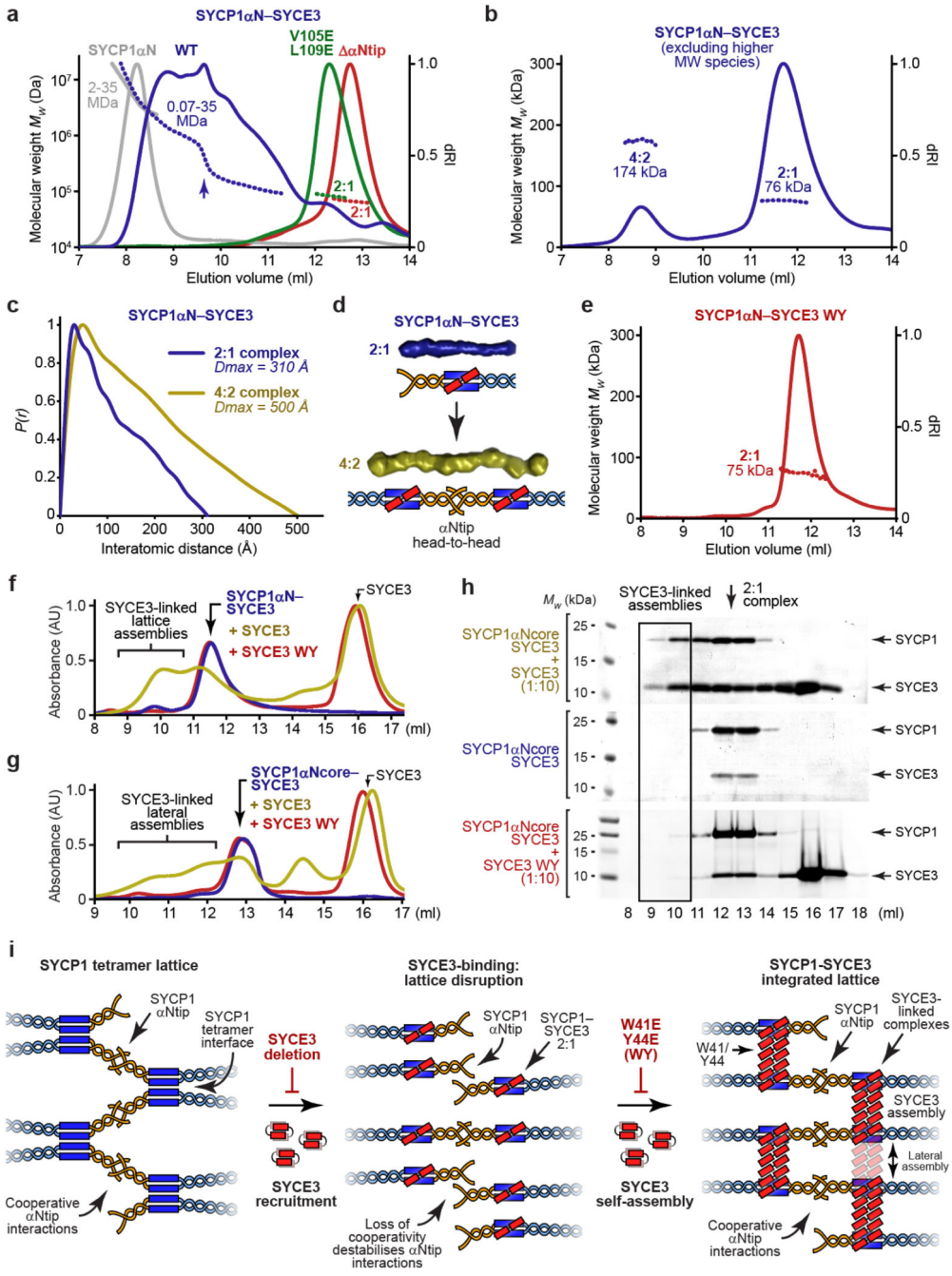

Fig. 3. SYCP1-SYCE3 forms an integrated lattice through SYCE3 self-assembly.

(**a,b**) SEC-MALS analysis. (**a**) SYCP1αN-SYCE3 (blue) forms large molecular weight species of 0.07-35 MDa (with a step from 200 kDa to 0.8 MDa indicated by an arrow), which are restricted to 2:1 complexes of 70 kDa and 75 kDa by SYCP1 ΔNtip (green) and SYCE3 WY (red) mutations, respectively; theoretical – 71 kDa and 74 kDa. SYCP1αN forms 2-35 MDa species (grey). (**b**) SYCP1αN-SYCE3 (purified by size-exclusion chromatography to exclude large molecular weight species) demonstrates discrete 2:1 and 4:2 complexes of 76 kDa and 174 kDa, respectively; theoretical – 74 kDa and 148

kDa. (**c**) SEC-SAXS *P(r)* distributions of SYCP1αN-SYCE3 2:1 (blue) and 4:2 (yellow) species, including their *Dmax* and *Rc* values, and (**d**) *ab initio* models shown alongside a schematic of 4:2 complex formation through αNtip-mediated head-to-head interaction of 2:1 molecules. (**e**) SEC-MALS analysis showing that SYCP1αN-SYCE3 WY is a 75 kDa 2:1 complex; theoretical – 74 kDa. (**f-h**) Size-exclusion chromatography of (**f**) 95 μM SYCP1αN-SYCE3 and (**g,h**) 95 μM SYCP1αNcore-SYCE3 upon incubation with a 10-fold stoichiometric excess (per molecule) of SYCE3 wild-type or WY, shown as (**f,g**) UV absorbance (280 nm) chromatograms normalised to the same maximum peak height, and (**h**) SDS-PAGE of elution fractions. Additional controls and elution fractions are shown in Extended Data Fig. 5a-c. (**i**) SYCP1's tetramer lattice depends on its tetramer and αNtip head-to-head interfaces. SYCE3 recruitment initially disrupts tetramer interfaces, forming 2:1 complexes that cannot support cooperative αNtip head-to-head interactions. Further SYCE3 molecules assemble, mediated by W41 and Y44 amino-acids (inhibited by the WY mutation), into structures that incorporate and link together SYCP1-SYCE3 complexes, mimicking tetramer associations to form an integrated SYCP1-SYCE3 lattice. SYCE3 assemblies may link together more than two SYCP1-SYCE3 complexes, providing the lateral assembly interactions observed for SYCP1αNcore-SYCE3, and possibly further stabilising the SYCP1-SYCE3 lattice.

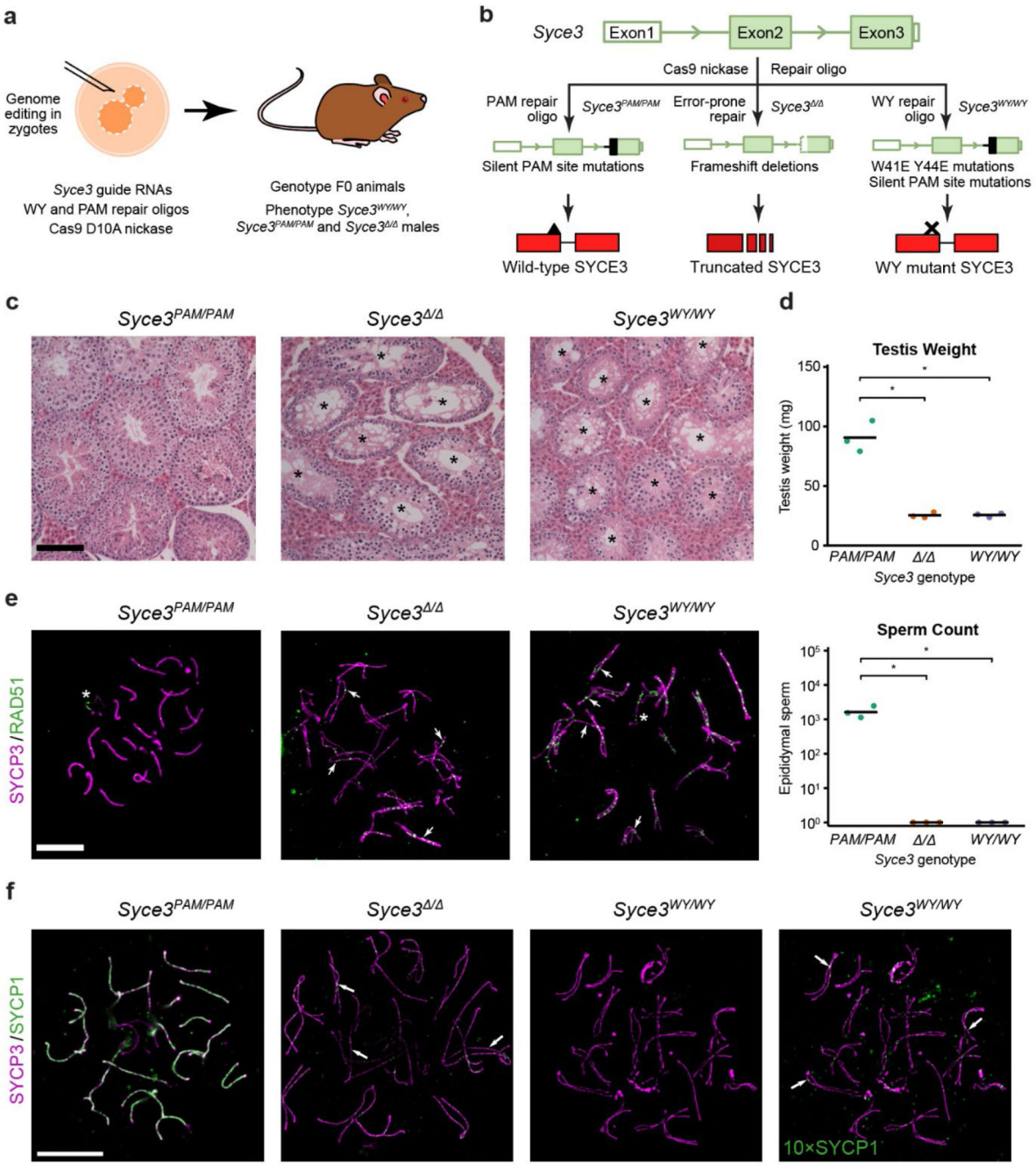

Fig. 4. SYCE3 self-assembly is required for SC assembly and meiotic progression *in vivo*.

(**a**) Generation and analysis of *Syce3* mutant mice. Zygotes were microinjected with *Syce3* CRISPR/Cas9 genome editing reagents and male F0 animals with desired genotypes analysed. (**b**) *Syce3* genome editing strategy. *Syce3* protein coding regions are filled green, regions repaired by the repair oligos are filled black, and their effects on SYCE3 protein (red) are indicated. (**c**) Haematoxylin and eosin staining of *Syce3* testes sections. Asterisks indicate tubules with a spermatogenic block and depletion of post-meiotic spermatids. Scale bar, 100 μm. (**d**) Testis weights (top) and sperm counts (bottom) of *Syce3* animals.

Europe PMC Funders Author Manuscripts

Testis weights for each animal are shown, with the mean for each genotype indicated with a black horizontal bar. Means are 90.6, 25.4 and 25.7 mg. *, $p<0.01$, (Student's t-test, n=3). Total numbers of sperm isolated from one epididymis per animal are plotted with the mean for each genotype indicated with a black horizontal bar. Means are 1709, 0 and 0 sperm. *, $p<0.05$ (Student's t-test, n=3). (**e,f**) Widefield imaging of pachytene *Syce3*$^{PAM/PAM}$ and asynapsed pachytene *Syce3*$^{\Delta/\Delta}$ and *Syce3*$^{WY/W}$ meiotic chromosome spreads immunostained for SYCP3 (magenta) and either RAD51 (**e**, green) or SYCP1 (**f**, green). Examples of paired asynapsed chromosomes are indicated with arrowheads (**e**), axial SYCP1 foci with arrows (**f**) and sex chromosomes with an asterisk. Scale bar, 10 μm.

Europe PMC Funders Author Manuscripts

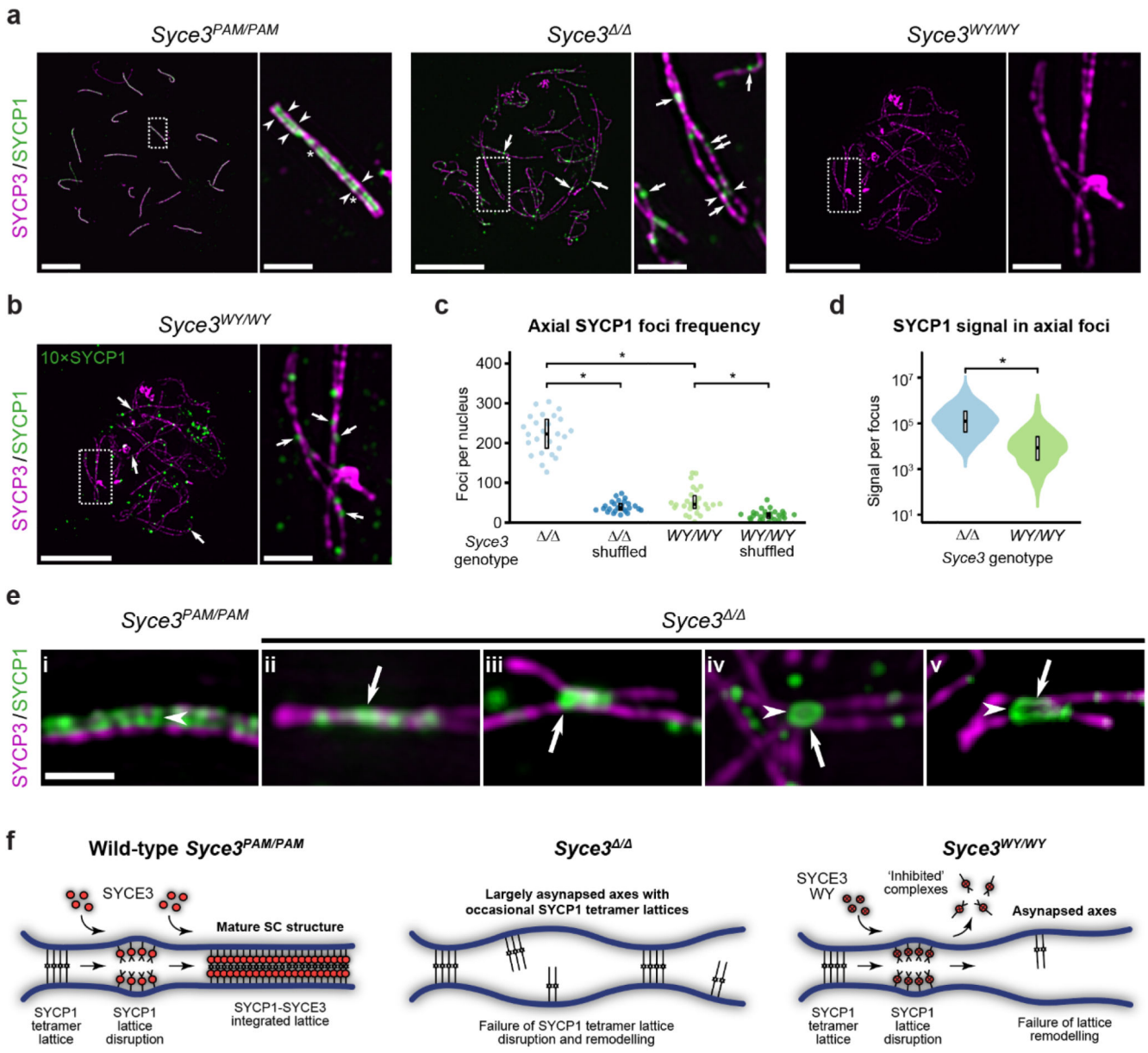

Fig. 5. SYCP1 tetramer lattices are disrupted by SYCE3 WY *in vivo*.

(**a,b**) SIM images of pachytene *Syce3*$^{PAM/PAM}$ and asynapsed pachytene *Syce3*$^{Δ/Δ}$ and *Syce3*$^{WY/WY}$ meiotic chromosome spreads immunostained for SYCP3 (magenta) and SYCP1 (green). The brightness of the SYCP1 channel in the *Syce3*$^{WY/W}$ image in (a) has been increased ten-fold to generate the image in (b). Example axial SYCP1 foci (arrows), chains of SYCP1 foci (arrowheads), and SYCP1 discontinuities (asterisks) are indicated. Example linear SYCP1 extensions are shown in Extended Data Fig. 7a. Scale bars, 10 μm for low magnification images, 1 μm for enlarged regions. (**c**) SYCP1 focus centroids within 35 nm of the SYCP3 axis mask in *Syce3* asynapsed pachytene nuclei were classed as axial (Extended Data Fig. 7b) and counted. Axial foci in shuffled datasets represent the median after twenty rounds of randomly assigning each SYCP1 focus centroid a location

within that nucleus. Crossbars represent quartiles; *, p<0.01 (Mann-Whitney U test, paired test used to compare observed with shuffled datasets, medians are 223, 37, 46 and 18.8 foci, n=25, 26 nuclei); 3 animals analysed for each *Syce3* genotype. (**d**) The total SYCP1 signal in each axial SYCP1 focus in (a) was measured. Crossbars represent quartiles; *, p< 0.01 (Mann-Whitney U test, nuclei medians are 127498 and 8600 arbitrary units, n=25, 26 nuclei); 3 animals analysed for each *Syce3* genotype. Data for individual animals are shown in Extended Data Fig. 7c. (**e**) SIM images of large extended SYCP1 assemblies at sites of close axes proximity in pachytene $Syce3^{PAM/PAM}$ (from Fig. 5a) and asynapsed pachytene $Syce3^{\Delta/\Delta}$ meiotic chromosome spreads immunostained for SYCP3 (magenta) and SYCP1 (green). Arrows indicate linear SYCP1 structures, arrowheads indicate central gaps between SYCP1 structures associated with paired axes. Scale bar, 1 μm. (**f**) Summary of the consequence of *Syce3* mutations. In wild-type and $Syce3^{PAM/PAM}$, nascent SYCP1 tetramer lattices are remodelled by wild-type SYCE3 protein into integrated SYCP1-SYCE3 lattices of mature SC structure. In $Syce3^{\Delta/\Delta}$, nascent SYCP1 tetramer lattices are retained by not matured owing to the absence of SYCE3. In $Syce3^{WY/WY}$, nascent SYCP1 tetramer lattices are disrupted but cannot be remodelled by SYCE3 WY, leaving largely undecorated axes.

Europe PMC Funders Author Manuscripts

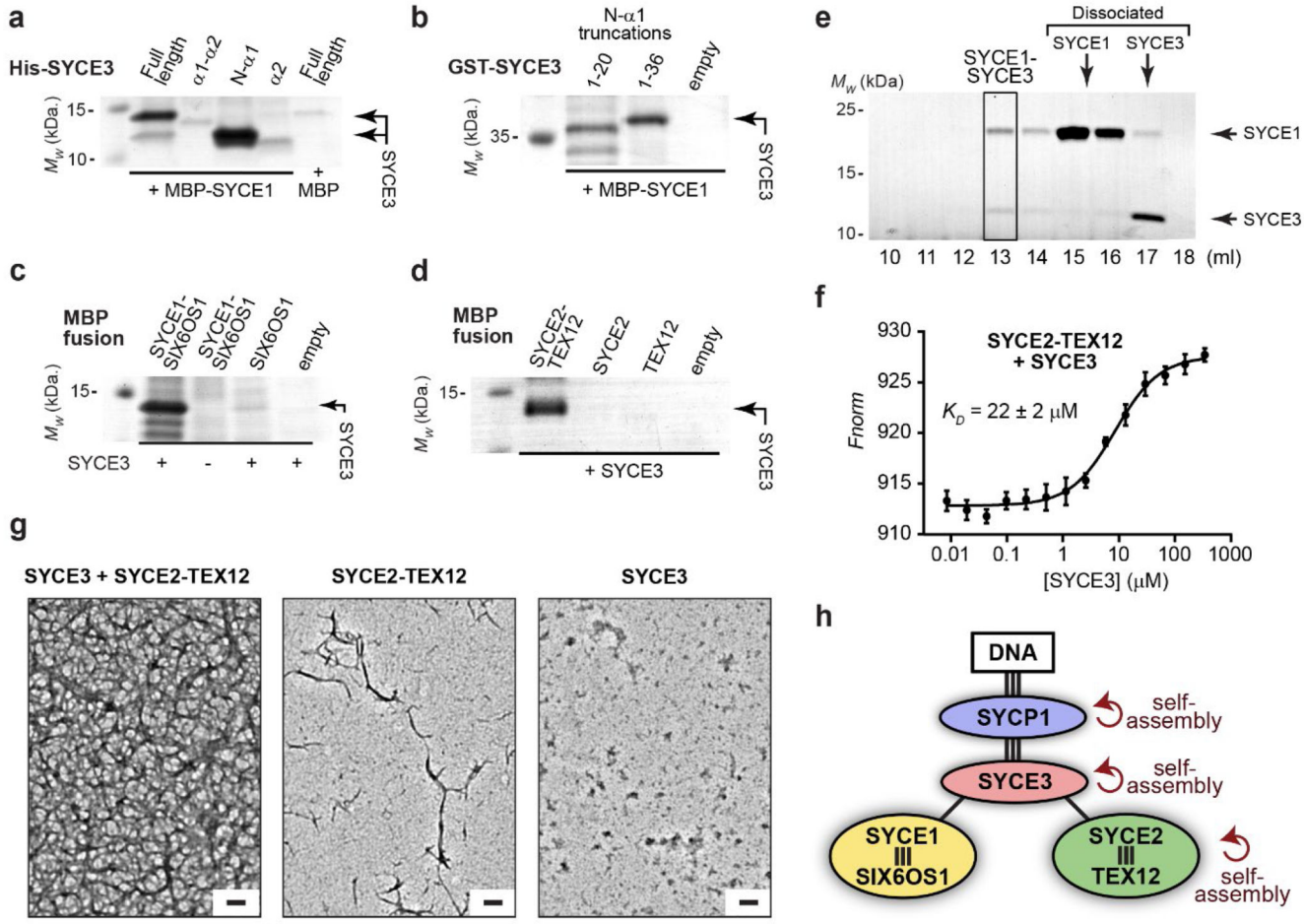

Fig. 6. SYCE3 interacts with SYCE1-SIX6OS1 and SYCE2-TEX12 central element complexes.

(**a-d**) Amylose pull-downs of (**a,c,d**) His-SYCE3 and (**b**) GST-SYCE3 and free GST (empty), following recombinant co-expression with (**a**) MBP-SYCE1core and free MBP (empty), (**b**) MBP-SYCE1core, (**c**) MBP-SIX6OS1N in the presence or absence of SYCE1core, and free MBP (empty), and (**d**) SYCE2-TEX12 core, SYCE2 core, TEX12 core and free MBP (empty). (**a**) SYCE3 constructs full-length, α1-α2, N-α1 and α2 correspond to amino-acids 1-88, 12-88, 1-52 and 54-88 (shown on the SYCE3 structure in Fig. 2c). (**e**) Size-exclusion chromatography of the SYCE1-SYCE3 complex, showing some complex retention (boxed) but mostly dissociation of components; UV chromatograms are shown in Extended Data Fig. 8a. (**f**) MST of SYCE3 titrated into 150 nM SYCE2-TEX12core, demonstrating an apparent binding affinity of 21.8 ± 2.1 μM (mean ± SEM, n=3 biologically independent replicates); full data are shown in Extended Data Fig. 8c-i. (**g**) Electron microscopy of SYCE2-TEX12 (full-length) following incubation with a two-fold molar excess of SYCE3; individual components are shown for comparison. Scale bars, 100 nm. Full panels are shown in Extended Data Fig. 9. (**h**) Interaction network of SC central element proteins, indicating strong interactions (three lines), weak interactions (single lines) and self-assembly.

Europe PMC Funders Author Manuscripts

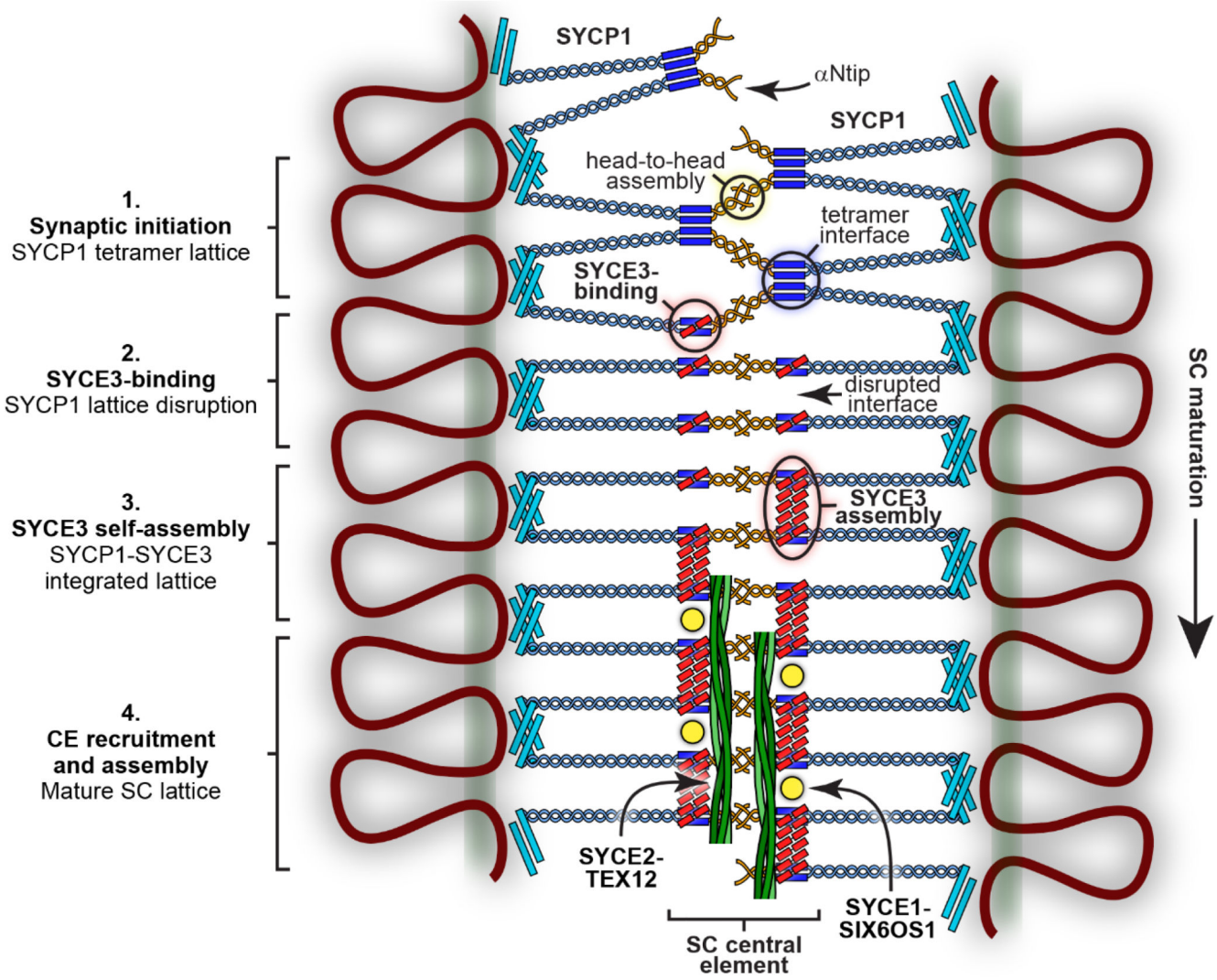

Fig. 7. Model for SC maturation through SYCP1 lattice remodelling and integration by SYCE3.

Model for the structural maturation of the SC through SYCE3-mediated remodelling of the SYCP1 lattice and recruitment of CE complexes. 1. Synaptic initiation and local lattice extension occur through the recruitment and assembly of SYCP1 tetramer lattices between chromosome axes. 2. SYCE3 recruitment disrupts the tetramer lattice by binding to SYCP1 dimers and competitively inhibiting the tetramer interface. 3. SYCE3 self-assembly then binds together SYCP1-SYCE3 complexes, mimicking the role of the tetramer interface, resulting in the remodelling of the initial SYCP1 tetramer lattice into an SYCP1-SYCE3 integrated lattice. 4. Incorporated SYCE3 assemblies recruit and initiate assembly of SYCE1-SIX6OS1 and SYCE2-TEX12 complexes that provide short-range and long-range fibrous supports that stabilise the SC's extension along the chromosome length.